CORRECTED 24 MAY 2024; SEE ERRATUM

SCIENCE ADVANCES | RESEARCH ARTICLE

CELL BIOLOGY

TREM2 inhibition triggers antitumor cell activity of myeloid cells in glioblastoma

Rui Sun[1], Rowland Han[1], Colin McCornack[1], Saad Khan[1], G. Travis Tabor[2], Yun Chen[2,3], Jinchao Hou[3], Haowu Jiang[4], Kathleen M. Schoch[2,5], Diane D. Mao[1], Ryan Cleary[1], Alicia Yang[1], Qin Liu[4], Jingqin Luo[6,7], Allegra Petti[1,8,9], Timothy M. Miller[2,5], Jason D. Ulrich[2,5], David M. Holtzman[2,5,10], Albert H. Kim[1,2,8,9,11]*

Triggering receptor expressed on myeloid cells 2 (TREM2) plays important roles in brain microglial function in neurodegenerative diseases, but the role of TREM2 in the GBM TME has not been examined. Here, we found that TREM2 is highly expressed in myeloid subsets, including macrophages and microglia in human and mouse GBM tumors and that high TREM2 expression correlates with poor prognosis in patients with GBM. TREM2 loss of function in human macrophages and mouse myeloid cells increased interferon-γ–induced immunoactivation, proinflammatory polarization, and tumoricidal capacity. In orthotopic mouse GBM models, mice with chronic and acute Trem2 loss of function exhibited decreased tumor growth and increased survival. Trem2 inhibition reprogrammed myeloid phenotypes and increased programmed cell death protein 1 (PD-1)$^+$CD8$^+$ T cells in the TME. Last, Trem2 deficiency enhanced the effectiveness of anti–PD-1 treatment, which may represent a therapeutic strategy for patients with GBM.

INTRODUCTION

Glioblastoma (GBM), the most common primary malignant brain tumor, continues to be a challenging disease, with short-term survival despite aggressive multimodal therapy (*1*). A major obstacle to effective GBM treatment is the "cold" tumor microenvironment (TME). Deficiencies in T cell infiltration and active proinflammatory responses render GBM resistant to many immunotherapies, including immune checkpoint blockade (*2*). Myeloid cell populations including macrophages and microglia, which account for more than 50% of leukocytes enriched in the TME (*3*, *4*), rarely exert tumoricidal functions and instead maintain an immunosuppressive microenvironment. The intrinsic phenotypic plasticity of myeloid cells contributes to adaptation to the brain's local inflammatory status and evolution into protumorigenic cell populations. Thus, approaches that remodel myeloid cell phenotypes are critical for developing new strategies for GBM treatment.

The myeloid cell receptor, triggering receptor expressed on myeloid cells 2 (TREM2), has been studied extensively for its function in microglia in neurodegenerative diseases such as Alzheimer's disease (*5*–*7*). Recently, studies have revealed that certain solid tumors express a high level of TREM2 (*8*–*11*), but the role of TREM2 in cancer appears to be tumor-type dependent. For instance, TREM2 suppressed the malignant progression of colorectal cancer and afforded protection from hepatocellular carcinoma (*8*, *9*). On the contrary, increased TREM2 expression in non–small cell lung and gastric cancers was associated with poor prognosis (*10*, *11*). One possible explanation for this inconsistency is that in some tumors, TREM2 can be expressed by cancer or stromal cells, which may result in differential effects on tumor progression (*12*). However, there is increasing evidence that TREM2 is widely expressed in tumor-associated macrophages, (*13*) and TREM2 loss of function altered the tumor macrophage landscape in the TME of solid tumors of the body, leading to improved efficacy of immune checkpoint blockade (*14*, *15*). However, little is known about the role of TREM2 in GBM progression and the mechanisms of how TREM2 regulates myeloid cell function (*16*).

RESULTS

TREM2 expression is higher in GBM tumors than normal brain tissue and inversely correlates with patient outcome

To determine the clinical relevance of TREM2 in human GBM, we first asked whether TREM2 expression is altered in *IDH1/2*–wild-type GBM tumors in The Cancer Genome Atlas. We found that TREM2 mRNA levels are significantly higher in *IDH1/2*–wild-type GBM tumors compared to normal brain tissue (Fig. 1A). We also found that in gliomas in general, TREM2 expression positively correlates with grade, with the highest levels found in grade 4 gliomas (fig. S1). To ascertain whether TREM2 levels are associated with clinical outcomes, we stratified *IDH1/2*–wild-type GBM tumors into high and low TREM2 expressers and found that high TREM2 expression correlates with shorter median progression-free survival (PFS) and overall survival (OS) (Fig. 1, B and C). To identify the specific cell type expressing TREM2 in GBM tumors, we examined our single-cell RNA sequencing (scRNA-seq) dataset using fresh tumor samples from two patients with GBM (*17*). As reported (*18*), among malignant tumor cells, there were four typical cellular

[1]Department of Neurological Surgery, Washington University School of Medicine, St. Louis, MO, USA. [2]Department of Neurology, Washington University School of Medicine, St. Louis, MO, USA. [3]Department of Pathology and Immunology, Washington University School of Medicine, St. Louis, MO, USA. [4]Department of Anesthesiology, Washington University School of Medicine, St. Louis, MO, USA. [5]Hope Center for Neurological Disorders, Washington University in St. Louis, St. Louis, MO, USA. [6]Department of Surgery, Washington University School of Medicine, St. Louis, MO, USA. [7]Division of Biostatistics, Washington University School of Medicine, St. Louis, MO, USA. [8]Department of Genetics, Washington University School of Medicine, St. Louis, MO, USA. [9]The Brain Tumor Center, Siteman Cancer Center, Washington University School of Medicine, St. Louis, MO, USA. [10]Center for Science and Engineering of Living Systems, Washington University in St. Louis, St. Louis, MO, USA. [11]Department of Developmental Biology, Washington University School of Medicine, St. Louis, MO, USA.
*Corresponding author. Email: alberthkim@wustl.edu

CORRECTED 24 MAY 2024; SEE ERRATUM

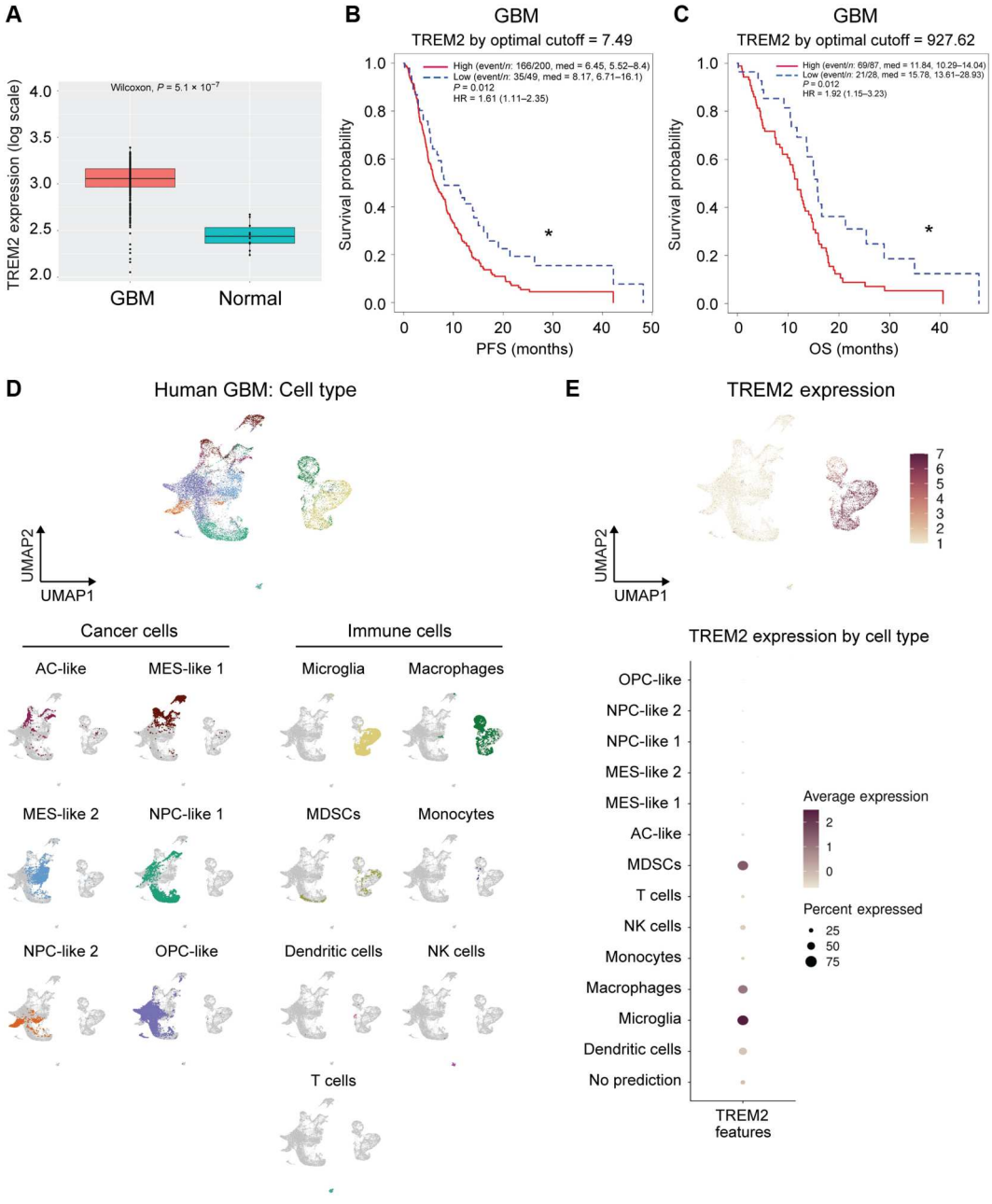

Fig. 1. TREM2 expression is higher in GBM tumors than normal brain tissue and inversely correlates with patient outcome. (**A**) Box plots of TREM2 expression in *IDH1/2*–wild-type GBM tumors ($n = 252$) and normal brain specimens ($n = 10$). Wilcoxon test, $P = 5.1 \times 10^{-7}$. (**B**) Kaplan-Meier curves show a PFS of 249 patients with *IDH1/2*–wild-type GBM based on TREM2 expression. TREM2 expression was dichotomized into high/low according to the optimal cutoff. Log-rank test, $P = 0.012$. (**C**) Kaplan-Meier curves show an OS of 115 patients with *IDH1/2*–wild-type GBM by high and low TREM2 expression. Patients were divided on the basis of the optimal cutoff of TREM2 expression. Log-rank test, $P = 0.012$. (**D**) UMAP plots of cell clusters identified in human GBM tumors. (**E**) UMAP and dot plots of TREM2 expression level in each cluster. AC, astrocyte; MES, mesenchymal; OPC, oligodendrocyte progenitor. *$P < 0.05$.

states, including astrocyte-, mesenchymal-, neural progenitor (NPC)–, and oligodendrocyte progenitor–like states (Fig. 1D). Among $CD45^+$ immune cells, unsupervised clustering by Uniform Manifold Approximation and Projection (UMAP) identified seven cell clusters corresponding to typical immune cell markers, such as microglia, macrophages, T cells, natural killer (NK) cells, and dendritic cells (Fig. 1D). Microglia and macrophages occupy the major fractions of leukocytes (Fig. 1D). In contrast to tumor cells, we found high expression of TREM2 in myeloid cell populations, including microglia, macrophages, and myeloid-derived suppressor cells (MDSCs) (Fig. 1E). Thus, in GBM, we hypothesized that TREM2-expressing tumor-associated myeloid populations might play important roles in tumor progression.

Mouse GBM tumors show abundantly infiltrated Trem2$^+$ myeloid cells

We explored the role of TREM2 using the *IDH1*–wild-type syngeneic mouse model SB28 (*19*), which recapitulates major characteristics of human GBM, such as resistance to radiotherapy and temozolomide treatment (*20*, *21*), resistance to immune checkpoint blockade, and high fraction of myeloid cells in the TME (*19*, *22*, *23*). Similar to human GBM tumors, scRNA-seq analysis of in vivo SB28 tumors revealed that macrophage/monocyte-lineage and microglial cells were predominant among all immune cell subsets (Figs. 1D and 2A). We further analyzed *Trem2* mRNA levels across all cell clusters and found that Trem2 was highly expressed by microglia, M2-like macrophages (CD204$^+$MRC1$^+$), and nonclassical monocytes (Ly6C^{low}CCR2$^-$), which play anti-inflammatory roles in tissue homeostatic regulation (Fig. 2B). Relatively low expression was found in M1-like interferon-γ (IFNγ)–induced cells and certain B cells (Fig. 2B). Notably, the microglial subset in both human and mouse GBM tumors expressed the highest levels of TREM2 (Figs. 1E and 2B). We examined the presence of myeloid cells in SB28 tumor in vivo by histopathology (Fig. 2C). An abundance of ionized calcium-binding adapter molecule 1 (Iba1)$^+$ cell populations, which mark both microglia and macrophages, was found to accumulate both inside and around tumor areas (Fig. 2D).

Trem2 loss of function in vivo inhibits tumor growth and prolongs animal survival

We found that there was no detectable Trem2 expression in mouse GBM cell line SB28 and an additional syngeneic mouse GBM cell line, NPA C54B (fig. S2A) (*24*). To address the function of Trem2-expressing myeloid cells in GBM tumor growth in vivo, we took advantage of Trem2 transgenic mice (Fig. 3A). Using both SB28 and NPA C54B orthotopic GBM models, *Trem2*$^{-/-}$ mice showed increased OS and slower tumor growth in vivo compared to tumor-bearing *Trem2*$^{+/+}$ mice (Fig. 3B and fig. S2B). Moreover, the average weight of tumors dissected from *Trem2*$^{-/-}$ mice was much lower than *Trem2*$^{+/+}$ mice following orthotopic injection of SB28 cells (Fig. 3C). No obvious sexual dimorphism in terms of animal survival was observed in SB28-bearing *Trem2*$^{-/-}$ mice (fig. S2C). There were more apoptotic cells in tumors from *Trem2*$^{-/-}$ mice than those from *Trem2*$^{+/+}$ mice by cleaved caspase 3 immunohistochemistry (Fig. 3D), suggesting that Trem2 deficiency in the TME inhibits tumor growth by increasing tumor cell death.

To assess the preclinical effect of Trem2 loss of function on GBM growth through an orthogonal approach, we performed intracerebroventricular (ICV) injection of *Trem2*$^{+/+}$ mice with Trem2-targeted antisense oligonucleotides (ASOs) to acutely knockdown Trem2 in the brain, a strategy that is potentially therapeutically relevant (*25*). We first validated that Trem2 ASO treatment substantially decreases Trem2 mRNA levels in frontal, parietal, occipital, and cerebellar regions of the brain 5 days after injection (fig. S2D). The current treatment paradigm of Trem2 ASO by single-dose ICV injection was shown to effectively knockdown Trem2 for up to 2 months in mouse brain (*25*). We evaluated Trem2 expression in tumor-associated myeloid cells 30 days after tumor cell implantation. Flow cytometric analysis revealed that both microglial (CD45$^+$CD11b$^+$Ly6C^{low}) and blood-lineage myeloid subsets (CD45$^+$CD11b$^+$Ly6C^{high}) associated with in vivo SB28 tumors displayed reduced Trem2 (fig. S2E). We then asked whether acute, brain-specific Trem2 reduction influences GBM tumor growth. Following a single ICV dose of Trem2 ASO (Fig. 3E), animals orthotopically injected with GBM cells demonstrated significantly increased survival in Trem2 ASO–treated mice compared to control (inactive) ASO–treated mice using both SB28 and NPA C54B cell models (Fig. 3E). Histological examination at 20 days after tumor cell injection showed that tumor size was diminished in Trem2 ASO–treated mice (Fig. 3E).

As a third approach to inhibiting Trem2 function, we used a TREM2 blocking antibody (clone: 178) that was reported to inhibit tumor growth in a mouse sarcoma model (*15*). To better recapitulate the patient scenario, TREM2 antibody was administered intraperitoneally 4 days after orthotopic injection of SB28 tumor cells and then given three more times every 4 days (Fig. 3F). Compared to isotype antibody, delayed anti-TREM2 antibody treatment also led to improved animal survival in SB28-bearing mice (Fig. 3F). Together, these convergent results using three different experimental approaches indicate that Trem2 loss of function in the TME inhibits tumor growth in preclinical models of GBM.

IFNγ-primed *Trem2*$^{-/-}$ bone marrow–derived macrophages show increased phagocytotic function and cytotoxicity against SB28 GBM cells

To dissect the role of different myeloid subsets in GBM progression, we generated bone marrow (BM)–derived macrophages (BMDMs) (*26*) from *Trem2* transgenic mice (Fig. 4A and fig. S3, A and B). We first evaluated the phagocytic function of BMDMs using fluorescently labeled beads (Fig. 4B). Although there was no difference in bead phagocytosis between untreated *Trem2*$^{+/+}$ and *Trem2*$^{-/-}$ BMDMs, following IFNγ treatment, *Trem2*$^{-/-}$ BMDMs showed a significant increase in phagocytic ability compared with *Trem2*$^{+/+}$ BMDMs (Fig. 4B). Macrophage conditioned medium (CM) has been demonstrated to reflect macrophage functions (*27*, *28*). We then tested the antitumor activity of CM derived from primary mouse BMDMs in vitro. Although CM from untreated BMDMs did not produce any measurable cytotoxicity in SB28 cells (fig. S3C), CM from IFNγ-primed *Trem2*$^{-/-}$ BMDMs caused notable cytotoxicity to SB28 cells, which was not observed in control IFNγ-primed *Trem2*$^{+/+}$ BMDMs (Fig. 4C). We also examined SB28 cell proliferation in a Transwell coculture system with no direct tumor cell contact with BMDMs. In this system, *Trem2*$^{-/-}$ BMDMs substantially suppressed tumor cell growth when supplemented with IFNγ compared to control *Trem2*$^{+/+}$ BMDMs (Fig. 4D). Consistently, *Trem2*$^{-/-}$ BMDMs secreted higher levels of nitric oxide (NO) compared to *Trem2*$^{+/+}$ BMDMs upon IFNγ treatment (Fig. 4E). We noticed that IFNγ directly decreased SB28 proliferation and increased tumor cell NO secretion, indicating that the SB28 model is intrinsically susceptible to IFNγ as with other cancer cells (fig. S3, D and E) (*29*, *30*), but the tumoricidal effects of IFNγ were further augmented by activated BMDMs in the context of *Trem2* deficiency (Fig. 4, C and D). To explore the mechanism of how Trem2 deficiency enhances antitumor effects in BMDMs, we examined the differentially expressed genes between *Trem2*$^{+/+}$ and *Trem2*$^{-/-}$ BMDMs responding to IFNγ or dead tumor cell stimulation using bulk RNA-seq (Fig. 4, F and G). IFNγ robustly induced the expression of several proinflammatory genes or M1-type markers in *Trem2*$^{-/-}$ BMDMs, such as *Tnf*, *Nos2*, *Cxcl10*, *Socs3*, and *Cd80* (Fig. 4F), consistent with increased tumoricidal function and NO secretion in *Trem2*$^{-/-}$ BMDMs (Fig. 4, C to E). Subnetwork analyses indicated that these

CORRECTED 24 MAY 2024; SEE ERRATUM

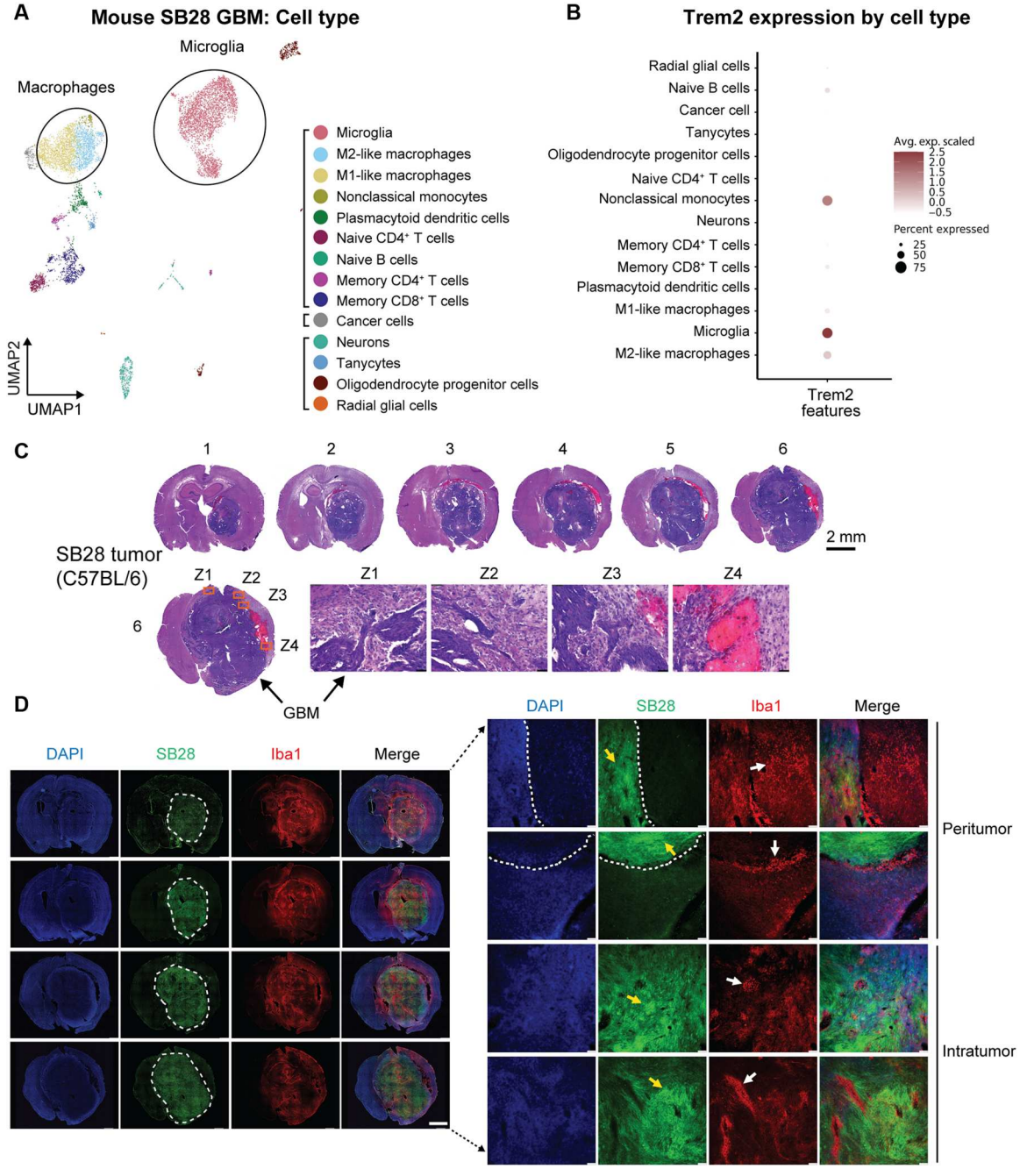

Fig. 2. Mouse GBM tumor shows abundant Trem2$^+$ myeloid cells in the TME. (**A**) UMAP plots of cell type clusters in mouse SB28 model of GBM in vivo. (**B**) Dot plots of TREM2 expression level in each cell cluster. (**C**) Representative histology of brain GBM (SB28). Cryosections of 30 μm thickness (1 to 6) by hematoxylin and eosin staining (top). Scale bar, 2 mm. Histological images for invasive tumor front on section 6: Z1, Z2, Z3, and Z4. Scale bar, 50 μm. (**D**) Representative immunostaining images. Whole-brain sections (left). Red, Iba1; green, SB28 tumor cells (tracking dye); blue, nucleus [4′,6-diamidino-2-phenylindole (DAPI)]. Scale bar, 2 mm. Iba1$^+$ myeloid cells around and inside the tumor (right). Arrows indicate SB28 cells (yellow) and Iba1$^+$ cells (white). Scale bars, 100 μm.

differentially expressed genes are highly enriched in tumor necrosis factor (TNF) and nuclear factor κB (NFκB) signaling pathway (Fig. 4G). In contrast, IFNγ treatment overall suppressed the expression of genes associated with the differentiation of MDSCs and protumorigenic macrophages (*31*–*33*) in *Trem2*$^{-/-}$ BMDMs, including *Cd44*, *Pkm*, *Pdk1*, *Ccr5*, and *Ccr1* (Fig. 4F). Upon treating BMDMs directly with dead GBM cells as antigen, we found much higher expression of activated myeloid cell markers including *Cd83*, *H2-T24*, and *Nampt* (*34*) in *Trem2*$^{-/-}$ BMDMs (Fig. 4F). Several chemokine receptors related with immune tolerance, including *Ccr1*, *Ccr3*, and *Ccr5*, were induced at much lower levels in *Trem2*$^{-/-}$ BMDMs than in *Trem2*$^{+/+}$ BMDMs (Fig. 4F). In addition, we observed a dramatically decreased expression of *Cd36*, *Lpl*, and *Itgam* in *Trem2*$^{-/-}$ BMDMs (Fig. 4F). Pathway analysis showed

CORRECTED 24 MAY 2024; SEE ERRATUM

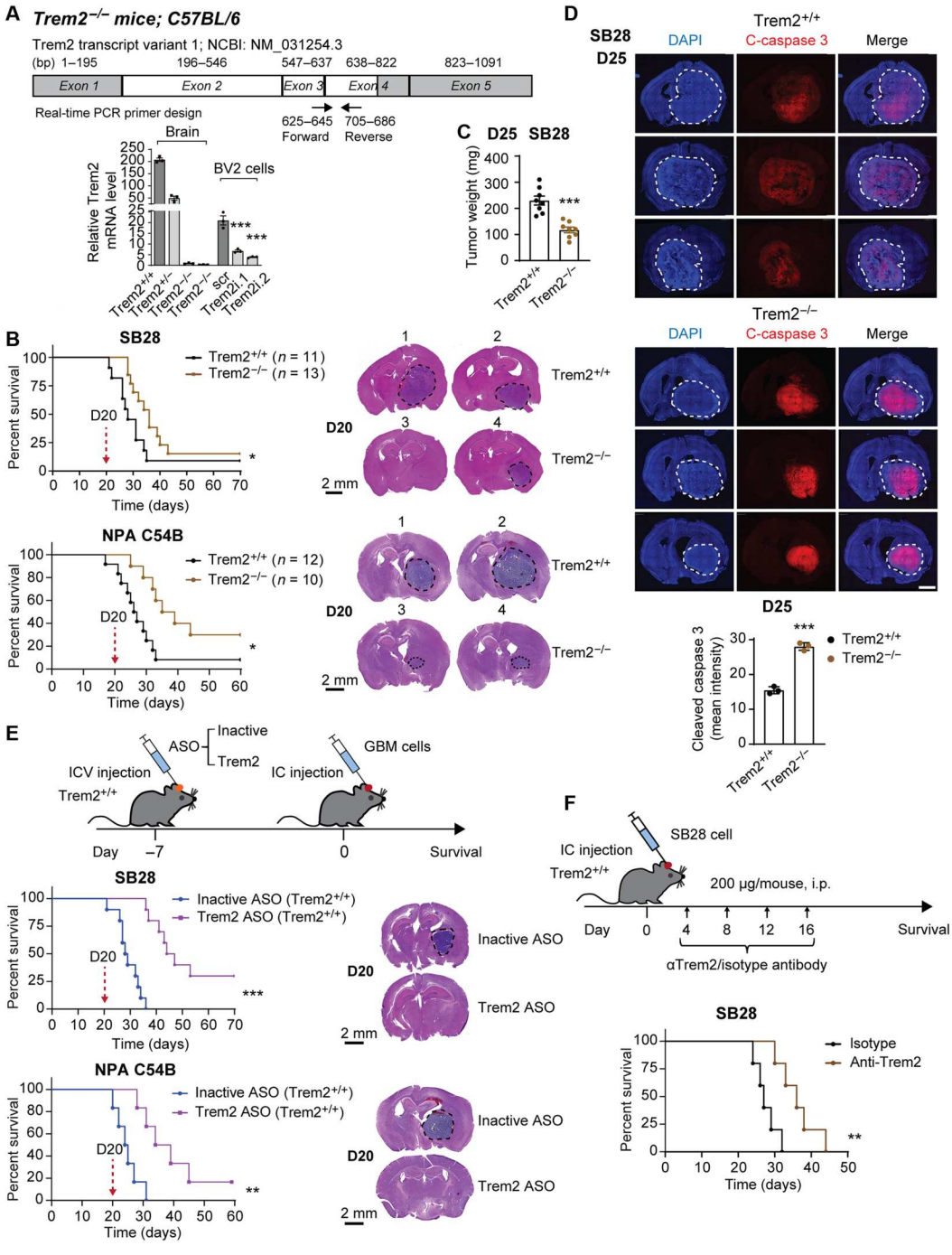

Fig. 3. Trem2 inhibition in vivo inhibits tumor growth and improves animal survival. (**A**) *Trem2*$^{-/-}$ mice genotype verified by real-time quantitative polymerase chain reaction (RT-qPCR) (n = 3). Primers' loci in *Trem2* mRNA were shown. *Trem2* mRNA detected in brain tissue from *Trem2*$^{+/+}$, *Trem2*$^{+/-}$, and *Trem2*$^{-/-}$ (*Trem2*$^{-/-}$_1 and *Trem2*$^{-/-}$_2) littermate mice. Control BV2 (scr) and Trem2 knockdown BV2 cells (Trem2i.1 or Trem2i.2) served the control. Comparisons performed as indicated. NCBI, National Center for Biotechnology Information. (**B**) *Trem2*$^{-/-}$ mice showed increased neurological deficit-free survival time than *Trem2*$^{+/+}$ mice in both SB28 and NPA C54B GBM models (left). Mice were euthanized at day 20 after tumor implantation. Representative histological images showing tumor size in *Trem2*$^{+/+}$ (1 and 2) and *Trem2*$^{-/-}$ (3 and 4) mice (right). Scale bars, 2 mm. (**C**) Tumor weight. SB28-bearing mice were euthanized at day 25. Whole-tumor mass was dissected and weighed (n = 8 per genotype). (**D**) Apoptotic cells in tumor tissue by cleaved caspase-3 (C-caspase 3) immunostaining (n = 3 per genotype). Quantified apoptosis shown as mean fluorescence intensity of tumor area (nuclei, DAPI) divided by C-caspase 3 intensity (red). Scale bar, 2 mm. (**E**) Acute Trem2 reduction by intracerebroventricular (ICV) injection of ASOs increased OS in GBM-bearing *Trem2*$^{+/+}$ mice. SB28, n = 10 per condition; NPA C54B, n = 6 per condition. Schematic showing experimental design (top). Kaplan-Meier curves demonstrated increased survival in animals injected with Trem2 ASO versus control ASO (inactive) (left). Mice were euthanized at day 20 after tumor implantation. Representative histological images showing tumor size (right). Scale bars, 2 mm. (**F**) Anti-Trem2 treatment increased animal survival in GBM-bearing mice (n = 5 per condition). *Trem2*$^{+/+}$ mice were injected intracerebrally (IC) with SB28 cells and treated intraperitoneally (i.p.) with anti-Trem2 or isotype antibody (200 μg per mouse). Experimental design (top). Survival curves (bottom). Data represent means ± SEM. *P < 0.05; **P < 0.01; ***P < 0.001.

that these genes regulate cholesterol metabolism and phagocytosis (Fig. 4G). In tumor-associated immune cells, CD36 has been shown to drive lipid-mediated metabolic reprogramming and functions to promote immune tolerance and cancer development (*35*). Lipoprotein lipase (LPL) was found to be associated with lipid uptake and an anti-inflammatory reparative phenotype in myeloid cells (*36*). Thus, we speculate that impaired lipid reprogramming in *Trem2*$^{-/-}$ BMDMs contributes to mitigation of the immunosuppressive phenotype. Together, we found Trem2 deficiency inhibits tolerogenic macrophage differentiation in response to both IFNγ and tumor antigen stimulation.

TREM2 knockdown in human macrophages enhances tumor cell kill in patient-derived GBM stem cells

To test the functional role of TREM2, we also took advantage of a human model system—patient-derived GBM stem cells (GSCs),

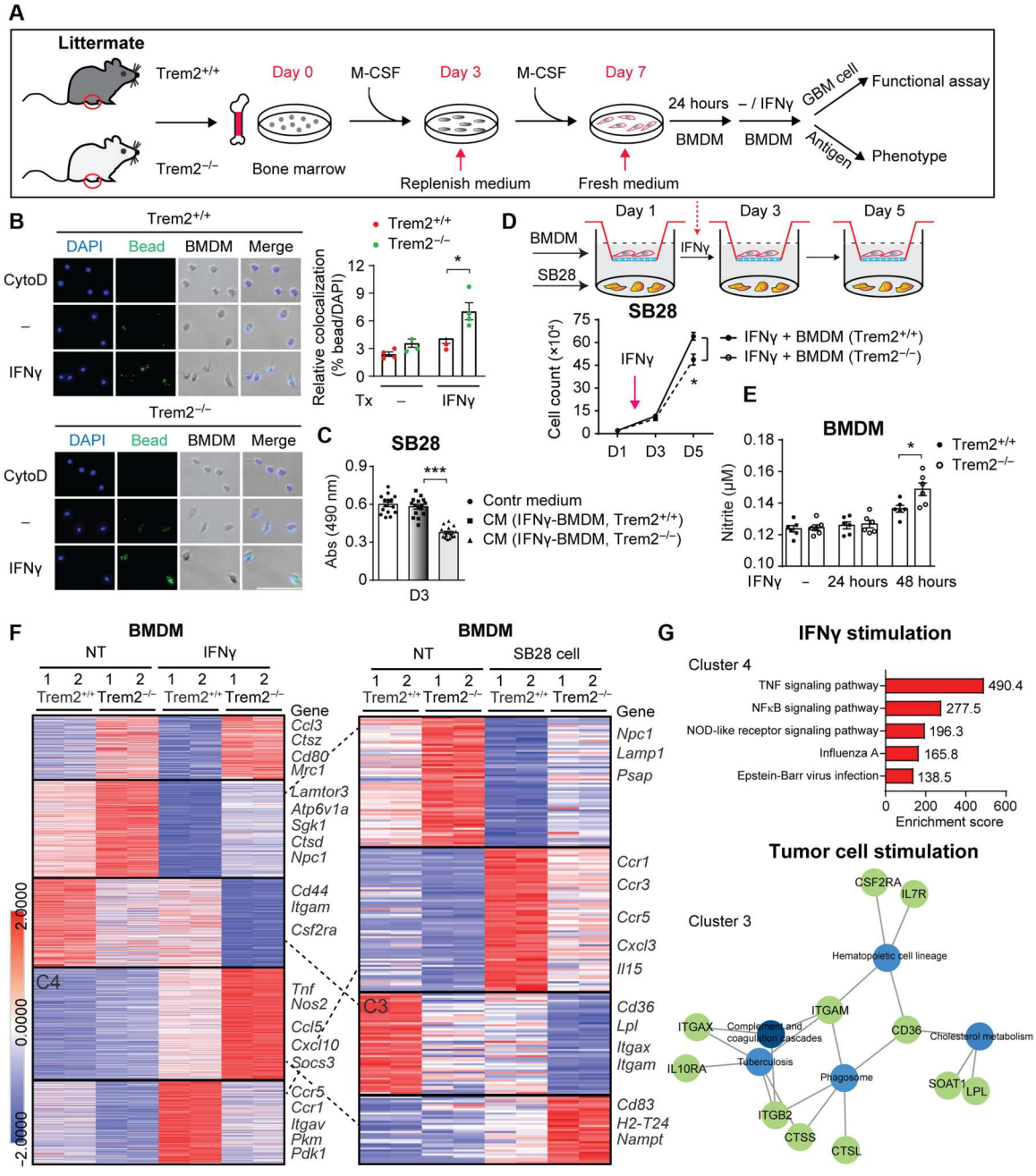

Fig. 4. Activated *Trem2*$^{-/-}$ BMDMs show increased phagocytosis and cytotoxic activity in killing GBM cells and proinflammatory phenotypes. (**A**) Schematic for BMDM induction from both *Trem2*$^{+/+}$ and *Trem2*$^{-/-}$ littermate mice. BM cells differentiated into macrophages following a 7-day macrophage colony-stimulating factor (M-CSF) induction. CM collected and used for cytotoxic assay as indicated. Gene expression was analyzed by bulk RNA-seq. (**B**) Phagocytosis of fluorescently labeled beads measured in BMDMs. BMDMs treated with phosphate-buffered saline (PBS) or IFNγ (10 ng/ml) for 30 min. Cytochalasin D (CytoD) was used as a negative control. Representative images (left). Scale bar, 100 μm. The colocalized ratio of beads in DAPI-positive cells (right; $n = 4$). (**C**) Cell viability of SB28 assessed by MTS assay. SB28 cells treated with CM from IFNγ-primed BMDMs on day 1. Cytotoxic effects examined on day 3 ($n = 16$ pooled from four independent experiments). Abs, absorbance. (**D**) Proliferative curves of SB28 cells. SB28 cells were cocultured with BMDMs by the number ratio of 1:2 in a Transwell system as shown. Absolute cell numbers of SB28 counted on days 1, 3, and 5 ($n = 3$). (**E**) Nitrite. BMDMs treated with IFNγ (10 ng/ml) and NO induction were assessed ($n = 6$). (**F**) Heatmaps of differentially expressed genes between *Trem2*$^{+/+}$ and *Trem2*$^{-/-}$ BMDMs ($n = 2$ per condition). BMDMs were treated with IFNγ (left) or tumor antigen (right) for 6 hours. (**G**) Enriched Kyoto Encyclopedia of Genes and Genomes (KEGG) pathways in cluster 4 upon IFNγ treatment (top, bar plot) and cluster 3 upon dead tumor cell stimulation (bottom). NOD, nonobese diabetic. Data represent means ± SEM. *$P < 0.05$; ***$P < 0.001$.

which we have generated and validated (*17*, *37*). Given prior evidence that TREM2 might be expressed in primary GBM cells (*38*), we examined TREM2 mRNA levels by real-time quantitative polymerase chain reaction (RT-qPCR) in these tumor cells in addition to human neural stem cells, human astrocytes, and the human monocyte cell line THP-1, the last as a positive control. Except for THP-1 monocytes, none of these cells expressed detectable levels of TREM2 (fig. S4A), indicating that TREM2 marks myeloid cell populations rather than tumor or neural cells, consistent with our scRNA-seq data. We further optimized and generated THP-1 monocyte-derived macrophage-like cells (fig. S4, B and C), which have been used as a valuable model for studying macrophage functions (*39*). We used lentivirus-mediated RNA interference (RNAi) to create stable TREM2 knockdown THP-1 macrophages, as well as nonsilencing control cells (fig. S5, A to C, and table S1). Assessment of cellular morphology and typical macrophage markers revealed no significant differences between control and TREM2 knockdown cells (fig. S5D), suggesting that TREM2 is not required for THP-1 monocyte-macrophage differentiation. We next investigated the ability of TREM2 to regulate macrophage-mediated cytotoxicity of human GSCs (Fig. 5A). Compared to control cells, both short-term (48 hours) and long-term (72 hours) CM taken from TREM2 knockdown macrophages in culture more robustly decreased GSC viability and increased their death, which was observed in two distinct human GSC lines (Fig. 5, B to E, and fig. S6, A to D).

We explored the components in CM from TREM2 knockdown macrophages that could induce tumor cell death. We first fractionated the 48-hour CM by molecular size and found antitumor activity was present in the 10- to 100-kDa fraction (fig. S6E). To determine the biochemical nature of the cytotoxic activity, we boiled the active fraction to denature proteins, which led to the loss of the cytotoxic effect on GSCs (fig. S6E). However, the active fraction treated with both ribonuclease (RNase) and deoxyribonuclease retained its capacity to induce GSC death (fig. S6E). Thus, these data indicate that secreted proteins likely mediate the antitumor activity of CM. Given that the proinflammatory cytokine TNFα, a 17-kDa protein, is mainly produced by activated macrophages and has pleiotropic effects on malignant cells, we examined the production of TNFα in CM. TREM2 knockdown macrophages secreted more TNFα than control cells in CM (fig. S6F). Furthermore, the cytotoxic effects of CM were decreased by addition of adalimumab, an anti-TNFα blocking antibody (fig. S6G). We also found that early addition of adalimumab into the culture medium of TREM2 knockdown macrophages triggered a more profound loss of cytotoxicity of CM compared to control cells (fig. S6H). Overall, these results suggest that an autocrine/paracrine TNFα-TNFR loop in TREM2 knockdown macrophages leads to secretion of antitumor proteins, among which include TNFα.

Macrophages are generally categorized as M1-like IFNγ-induced macrophages and M2-like suppressive macrophages. TREM2 has been shown to inhibit mouse macrophage activation (*40*). We thus investigated TREM2's role in IFNγ-induced adaptive immune responses in THP-1–derived human macrophages. IFNγ-treated CM from TREM2 knockdown macrophages showed higher cytotoxicity against GSCs under both acute (24 hours) and chronic (48 hours) conditions (Fig. 5, F and G). Moreover, upon 24 hours of IFNγ treatment, the expression of costimulatory molecules (*CD80* and *CD86*), proinflammatory cytokines (*TNFA* and *ILB*), *NOS2*, and IFN-stimulated genes (ISGs) (*CXCL10* and *SOCS1*) was significantly more increased in TREM2 knockdown macrophages, and M2-phenotype gene induction such as *MRC1* and *TGM2* was much lower than in control cells (fig. S7, A and B, and table S2). *CCL18*, which attracts naïve T cells and regulatory T cells (*41*, *42*), was found to be highly up-regulated in TREM2 knockdown macrophages (fig. S7, A and B, and table S2), implying homeostatic regulation to avoid excessive inflammation. These data suggest that TREM2 acts to hinder IFNγ-mediated immunoactivation and TREM2 inhibition promotes M1-like phenotype induction upon IFNγ treatment in human macrophages (fig. S7C).

We further examined the role of TREM2 in M2-phenotype polarized macrophages upon interleukin-4 (IL-4) and IL-13 treatment (fig. S8A). As opposed to the M1-polarized macrophages, we found that CMs from both TREM2 knockdown and control macrophages increase GSC viability (fig. S8B). Analysis of phenotypic gene expression revealed that mRNA levels of M2-phenotype genes were highly induced in control cells, such as *MRC1*, *TGM2*, *CCL18*, and *IL22*, and expression of most M1-pheotype genes, including *TNFA* and *IL1B*, were not increased in both control and TREM2 knockdown cells (fig. S8C). Several M2-phenotype genes including *IL10*, *TGFB*, *MRC1*, and *CCL18* were found to be highly increased in control cells compared to TREM2 knockdown cells (fig. S8C). In addition, *TREM2* mRNA levels were strongly induced in control M2-like macrophages (fig. S8C). Thus, although TREM2 knockdown restrains M2-phenotype polarization in human macrophages, M2-polarized macrophages appear to promote tumor growth in a manner independent of TREM2.

Trem2 loss-of-function microglia show increased phagocytic function, tumoricidal activity, and proinflammatory phenotype

Microglia are brain-resident macrophages, are distinct from those arising from the blood lineage, and have specialized roles in normal brain functions and brain diseases (*43*). We next asked whether Trem2-deficient microglial cells might contribute to inhibition of tumor growth in vivo (Fig. 3). We used the model of adoptive BM transplant to nonconditioned mice, which has advantages over myeloablation techniques in that the local environments of organs are protected and the hematopoietic niche is preserved. Chimeric BM *Trem2* transgenic mice (CD45.2$^+$) were generated by adoptive transfer of allogeneic BM cells through retro-orbital injection (fig. S9A). Using the SB28 GBM model, we found that *Trem2*$^{-/-}$ mice with transplanted *Trem2*$^{+/+}$ BMs demonstrated a moderate but significant survival advantage compared to Trem2$^{+/+}$ mice with transplanted Trem2$^{-/-}$ BMs (fig. S9B). Consistently, smaller tumors were observed in SB28-bearing Trem2$^{-/-}$ mice with chimeric BM at day 20 after tumor implantation (fig. S9C). We also observed a large quantity of Iba1$^+$ myeloid infiltrates in both Trem2$^{+/+}$ and Trem2$^{-/-}$ mice with chimeric BMs at day 25 after tumor injection (fig. S9D), implying a phenotype switch rather than a change in myeloid cell number. These results suggest that Trem2-deficient resident microglia also play a substantial role in tumor suppression in vivo. To better understand the antitumor role of Trem2-deficient microglia, we used the BV2 cell line, a commonly used model of microglial function (44). Trem2 knockdown in BV2 cells was confirmed using both lentiviral transduction and Trem2 ASO treatment (Fig. 6, A and C). We measured the phagocytic activity in both RNAi-transduced BV2 cells and ASO-treated BV2 cells using an in vitro bead assay. Under both conditions,

CORRECTED 24 MAY 2024; SEE ERRATUM

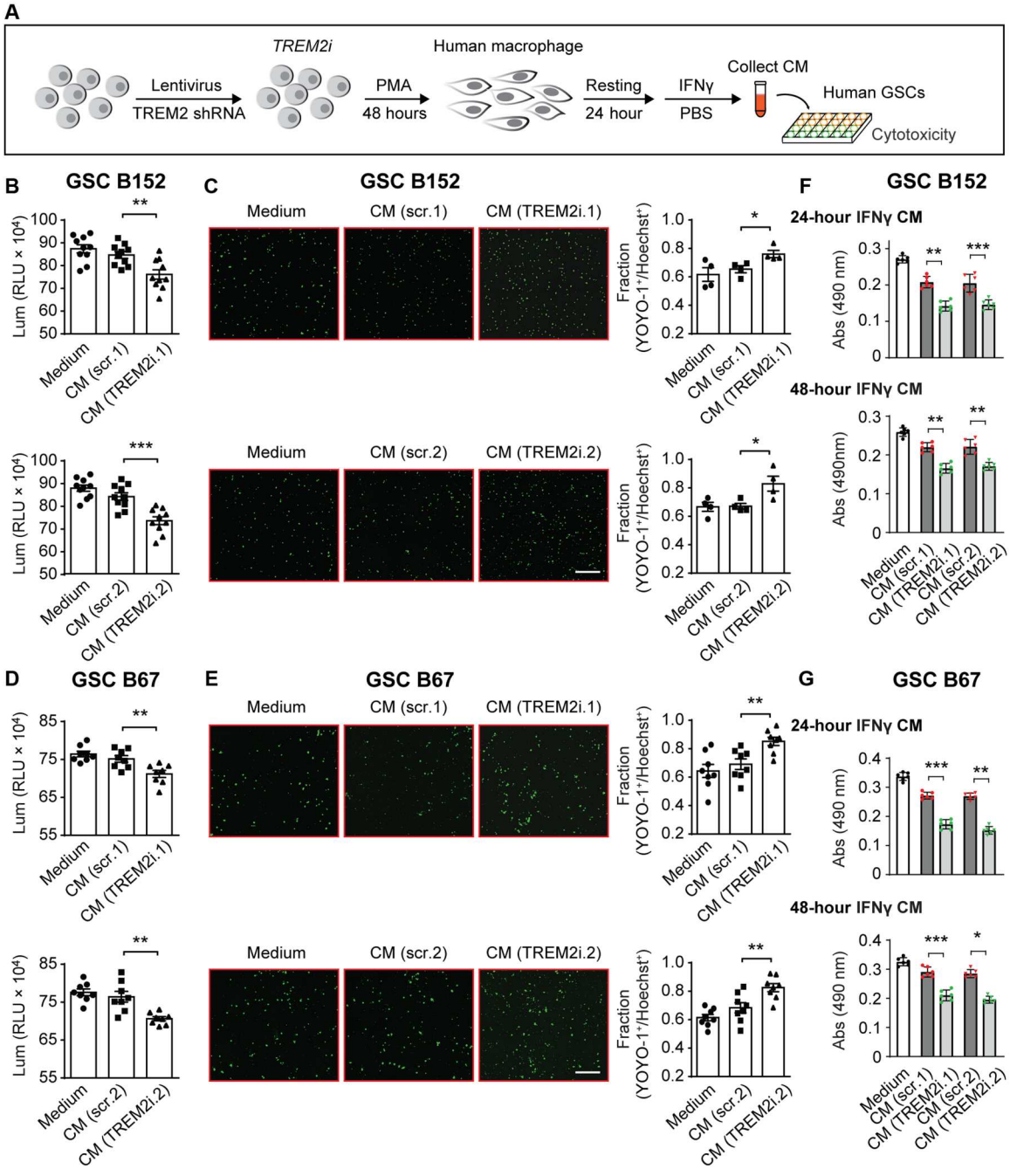

Fig. 5. TREM2 knockdown human macrophages demonstrate enhanced cytotoxic effects on human GSCs. (**A**) TREM2 knockdown THP-1–derived macrophages and their antitumor function. Human THP-1 monocytes were stably transduced with TREM2-targeted or control short hairpin–mediated RNA (shRNA) lentivirus. Macrophage differentiation was induced by 100 nM phorbol 12-myristate 13-acetate (PMA) for 48 hours. After 24 hours of resting, cells were continually cultured for another 48 hours in fresh medium or treated with IFNγ (20 ng/ml) for 24 or 48 hours, respectively. CM was collected. (**B** to **E**) GSCs B152 and B67 treated with CM (48 hours) from cultured THP-1 macrophages for 48 hours. Complete medium used as a control. (B) and (D) Cell viability shown as luminescence intensity (RLU) detected by adenosine 5by ty shown as (ATP) assay. GSCs B152 ($n = 10$) and B67 ($n = 8$). (C) and (E) Cell death shown as positive YOYO-1 staining (green fluorescence). Representative images (left). Scale bars, 100 μm. Death ratio quantified as particle fraction of nuclei (Hoechst) divided by YOYO-1 (right). GSCs B152, $n = 4$; B67, $n = 8$. scr, scrambled; Lum, luminescence. (**F** and **G**) Viable cells detected as absorbance at 490-nm wavelength by MTS assay. GSCs B152 and B67 treated with CM from IFNγ-stimulated THP-1 macrophages for 48 hours. Complete medium with IFNγ served the control. (F) GSCs B152 ($n = 6$ per condition). (G) GSCs B67 ($n = 6$ per condition). Data represent means ± SEM. *$P < 0.05$; **$P < 0.01$; ***$P < 0.001$.

CORRECTED 24 MAY 2024; SEE ERRATUM

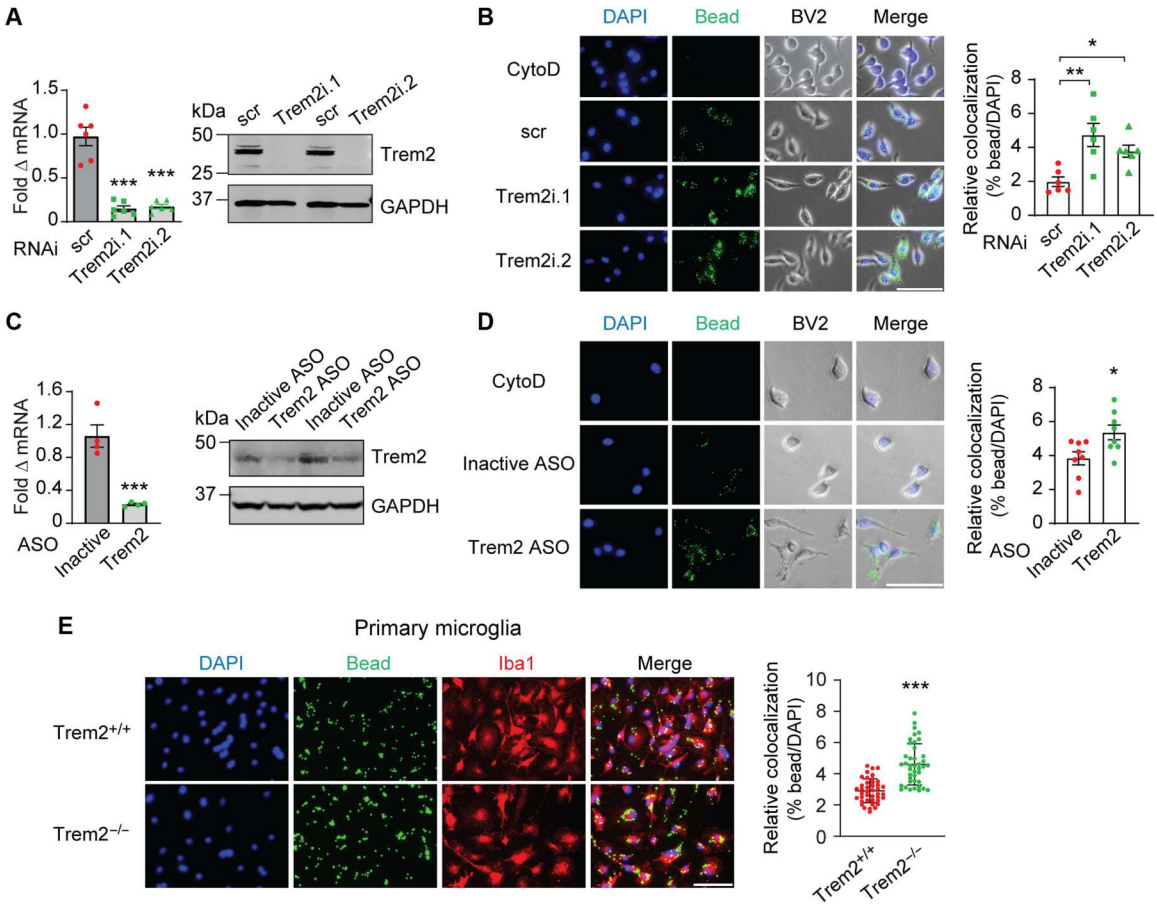

Fig. 6. Trem2-deficient microglial cells demonstrate increased phagocytotic activity. (**A** to **D**) Phagocytosis of fluorescently labeled beads was measured in BV2 cells. (A) Trem2 expression. Trem2 knockdown in BV2 cells by lentivirus transduction: Trem2-targeted shRNA (Trem2i.1 and Trem2i.2) and nonsilencing shRNA (scr). Fold change of Trem2 mRNA (left; $n = 6$). Representative Western blot (right, $n = 2$). (B) Phagocytotic activity. Cytochalasin D, an inhibitor of actin polymerization, was used as a negative control. Representative images (left). Scale bar, 100 μm. The colocalized ratio of beads in DAPI-positive cells (right; $n = 6$). (C) Trem2 expression. BV2 cells treated with inactive or Trem2-targeted ASO for 48 and 72 hours, respectively. Fold change of Trem2 mRNA (left; $n = 4$). Representative Western blot (right; $n = 2$). (D) Phagocytotic activity. Cytochalasin D served the control. Representative images (left). Scale bar, 100 μm. Quantified colocalization of beads with DAPI-positive cells (right; $n = 8$). (**E**) Phagocytosis of fluorescently labeled beads measured in primary microglia. Primary microglia isolated from *trem2* transgenic mice. Representative images (left). Scale bar, 100 μm. The colocalized ratio of beads in DAPI-positive cells (right; $n = 41$ fields per condition). Data represent means ± SEM. $^{*}P < 0.05$; $^{**}P < 0.01$; $^{***}P < 0.001$.

Trem2 knockdown BV2 cells showed a significant increase in their ability to engulf fluorescently labeled beads compared with control cells (Fig. 6, B and D). We then isolated and cultured primary microglia (45) from Trem2 transgenic mice (Fig. 6E). Similar to BV2 cells, Trem2$^{-/-}$ primary microglia showed increased phagocytotic capacity of fluorescently labeled beads (Fig. 6E).

We next examined BV2-mediated anti-GBM function using CM from naïve or IFNγ-polarized BV2 cells (Fig. 7A). Compared to control cells, both short-term (48 hours) and long-term (96 hours) CM from Trem2 knockdown BV2 cells demonstrated greater cytotoxicity on SB28 GBM cells (Fig. 7B). CM from IFNγ-treated control BV2 cells led to higher tumor cell kill in SB28 cells compared to untreated CM (Fig. 7B). In addition, CM from IFNγ-treated Trem2 knockdown BV2 cells showed greater antitumor effects compared to that of IFNγ-treated control cells (Fig. 7B). We also monitored SB28 cell proliferation and viability through indirect contact coculture experiments with BV2 microglia (Fig. 7C). Trem2 knockdown BV2 cells significantly inhibited the proliferation and viability of SB28 tumor cells with the addition of IFNγ (Fig. 7D). We further isolated primary microglia from *Trem2*$^{+/+}$ mice and treated these cells with ASOs. After Trem2 ASO treatment, mRNA and protein levels of Trem2 in primary microglia were markedly decreased (fig. S10A). As in our BV2 experiments, we collected CM from ASO-treated primary microglia. Both short-term (48 hours) and long-term (72 hours) CM from Trem2 ASO–treated primary microglia demonstrated greater cytotoxicity on SB28 cells than control ASO–treated cells (Fig. 7E). We then analyzed the antitumor effects of CM from IFNγ-treated primary microglia on tumor cells. Both Trem2 ASO– and control ASO–treated primary microglia could be activated by IFNγ, showing increased phosphorylation in signal transducers and activators of transcription 1 (STAT1) (fig. S10B). CM from IFNγ-treated microglia with reduced Trem2 was more effective in suppressing tumor cell growth compared to that of control treated cells (Fig. 7F).

To elucidate the mechanism of these findings, we first examined the resting microglial phenotype in BV2 (table S3). Upon Trem2 knockdown, the expression of a panel of microglial cell surface maker genes were not altered, including *Cd38*, *Cd68*, *Cd169*,

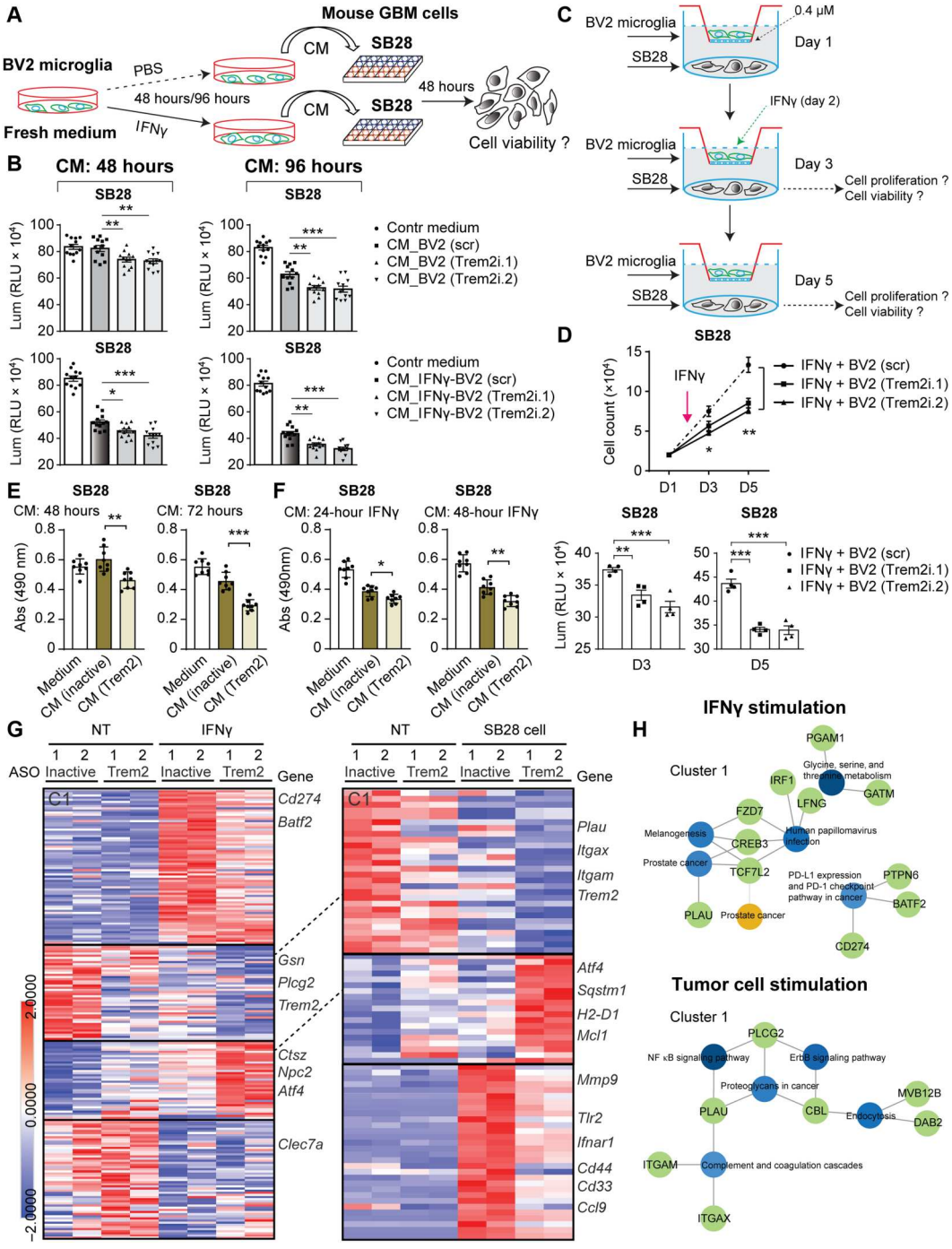

Fig. 7. Trem2-deficient microglia exhibit increased tumoricidal activity and proinflammatory phenotype. (**A** to **D**) Trem2 knockdown BV2 microglia were generated using Trem2-targeted shRNA lentivirus transduction (Trem2i.1 and Trem2i.2). Nonsilencing shRNA transduced cells were used as control (scr). (A) Schematic for the experimental strategy. CM was collected from untreated or IFNγ-treated BV2 cells. The cytotoxicity of CM on SB28 cells was assessed. (B) Cell viability detected as luminescence intensity. Top, untreated; bottom, IFNγ-treated; left, 48-hour CM; right, 96-hour CM (n = 12 pooled from three independent experiments). (C) and (D) Indirect antitumor effects of BV2 microglia assessed. (C) Experimental design for Transwell BV2-SB28 coculture. (D) Proliferative curve and cell viability. SB28 proliferation detected by absolute cell count (left; n = 3). Viable cells examined by ATP assay (right; n = 4). (**E** to **H**) Primary microglia treated with inactive (control) or Trem2-targeted ASOs for 72 hours. (E) The cytotoxicity of CM on SB28 cells assessed by MTS assay. CM collected from primary microglia following ASO treatment. Left, 48-hour CM (n = 8); right, 72-hour CM (n = 8). (F) Cytotoxic effects of IFNγ-treated CM on SB28 cells. After ASO treatment, primary microglia were stimulated with IFNγ (10 ng/ml) for 24 or 48 hours, and CM was collected (n = 8). (G) Heatmaps of differentially expressed genes between inactive and Trem2 ASO–treated primary microglia (n = 2 per condition). Primary microglia were treated with IFNγ (left) or dead SB28 cells (right) for 6 hours. (H) KEGG pathway enrichment analysis of cluster 1. Networks: IFNγ treatment (top) and tumor antigen treatment (bottom). Data represent means ± SEM. *P < 0.05; **P < 0.01; ***P < 0.001.

Cd204, *Mrc1*, *Tmem119*, *P2ry12*, and *Cx3cr1* (fig. S10C). Following IFNγ treatment, both control and Trem2 knockdown BV2 cells converted into amoeboid-like cells and the proliferative rates were similarly decreased (fig. S10, D and E). However, upon IFNγ stimulation, Trem2 knockdown augmented M1-phenotype polarization in BV2 cells: gene expression involved in antigen presentation (*Cd80* and *Cd86*), immune cell recruitment (*Ccl2* and *Cxcl9*), and inflammation (*Il6* and *Nos2*) was more increased; expression of *Cx3cr1*, *Mrc1*, and *Arg1* was further decreased compared to control cells (fig. S10F). Moreover, TNFα and NO secretion in Trem2 knockdown BV2 cells was higher than in control cells following IFNγ treatment (fig. S10, G and H). Together, Trem2 loss of function up-regulates IFNγ-induced proinflammatory potential in BV2 microglia.

To understand the antitumor phenotype of Trem2 loss-of-function microglia in a more unbiased fashion, we analyzed the transcriptomic profiles of ASO-treated primary microglia by RNA-seq (Fig. 7, G and H). Upon IFNγ treatment, Trem2 ASO–treated cells showed much lower induction of *Cd274* and *Batf2* than inactive ASO-treated cells (Fig. 7G), suggesting stronger activation of immunosuppressive pathways (*46*) in control primary microglia (Fig. 7H). The expression of *Gsn*, *Clec7a*, and *Plcg2* was markedly inhibited in Trem2 ASO–treated primary microglia (Fig. 7G). Gelsolin (GSN) plays an anti-inflammatory role by binding to inflammatory mediators, and phospholipase C gamma 2 (PLCG2) is required for TREM2-initiated signaling in microglia (*47*). Dectin-1 (*Clec7a*) drives immunosuppressive macrophage differentiation in the TME (*48*). Moreover, compared to control cells, gene expression of *Ctsz*, *Npc2*, and *Atf4* was highly induced in Trem2 ASO–treated primary microglia (Fig. 7G). Cathepsin Z (CTSZ) and NPC2 (*49*) play roles in regulating endosomal/lysosomal function, such as cholesterol trafficking and antigen presentation, and are highly expressed in M1-type macrophages. Activating transcription factor 4 (ATF4), a transcription factor, participates in proinflammatory cytokine and chemokine production, such as IL-6 and monocyte chemoattractant protein-1 (MCP-1) (*50*). Together, Trem2 ASO–treated primary microglia demonstrated a much more immunoactive phenotype upon IFNγ stimulation. We further treated primary microglia with dead tumor cells to explore their responses to tumor antigens (Fig. 7G). We found that Trem2 ASO–treated microglia exhibited relatively low expression of *Plau*, *Itgax*, and *Itgam* (Fig. 7G). Kyoto Encyclopedia of Genes and Genomes (KEGG) pathway analysis indicated that these genes are involved in the NFκB signaling pathway, phagocytosis of apoptotic cells or immune complexes, and cancer progression (Fig. 7H). Upon tumor cell treatment, we found a highly induced cluster of genes in Trem2 ASO–treated microglia, including *H2-D1*, *Atf4*, *Sqstm1* (*51*), and *Mcl1* (*52*) (Fig. 7H), which are associated with increased capacity for antigen presentation, cytokine induction, and proinflammatory phenotype polarization. Conversely, compared to control microglia, Trem2 ASO–treated microglia showed much lower expression of *Cd44*, *Cd33*, *Ccl9*, *Mmp9*, *Ifnar1*, and *Tlr2* (Fig. 7H), most of which are related with M2-type macrophage polarization and immunosuppressive myeloid subset induction. Together, these data demonstrate Trem2 inhibition promotes immunoactive microglial differentiation.

Trem2 loss-of-function microglial cells decrease tumor growth in coculture and tumor initiation in vivo

We next evaluated the direct tumoricidal activity of Trem2 loss-of-function myeloid cells both in vitro and in vivo (Fig. 8). We first evaluated the antitumor activity of Trem2 knockdown BV2 microglial cells, using a coculture system (Fig. 8A). We observed that coculture of control BV2 cells with SB28 cells led to substantial expansion of tumor cells and little, if any, growth of BV2 microglia by day 5 (Fig. 8B). However, coculture of Trem2 knockdown BV2 cells with SB28 cells resulted in notable inhibition of tumor cell growth and expansion of microglial cells (Fig. 8, B and C). To understand how Trem2 knockdown increases tumor cell kill and microglial expansion, we first examined TNFα production in the coculture system and found higher TNFα secretion in cocultures using Trem2 knockdown BV2 cells (fig. S11A). We then analyzed the expression of B-cell lymphoma 2 (Bcl-2) and Bcl-2 associated X (Bax) in BV2 cells, which reflect cell intrinsic survival signals (*53*, *54*). We found Trem2 knockdown BV2 cells exhibit a much higher ratio of Bcl-2 to Bax than control cells, suggesting that Trem2 inhibition enhances the survival capacity of BV2 microglial cells (fig. S11B). We also cocultured primary microglia with SB28 cells in vitro and similarly found that the growth rate of tumor cells cocultured with $Trem2^{-/-}$ microglia was lower than those cocultured with $Trem2^{+/+}$ microglia (fig. S11C), in line with the results with BV2 cells.

We then investigated the signaling pathways that Trem2 may modulate in microglial cells using BV2 cells. Upon IFNγ treatment, we found STAT1 activation was decreased in Trem2 knockdown BV2 microglia (fig. S12, A and B). Moreover, altered mitogen-activated protein kinases (MAPKs) and NFκB pathway activation was observed in Trem2 knockdown BV2 microglia upon lipopolysaccharide (LPS) treatment (fig. S12C). Both extracellular signal–regulated kinase (ERK) and c-Jun N-terminal kinase (JNK) activation were decreased, while MAPK p38 activity was increased in Trem2 knockdown BV2 microglia (fig. S12, C and D). Phosphorylated inhibitor of NFκBα (IκBα) demonstrated an increase at baseline in Trem2 knockdown BV2 cells although stimulated activity was unchanged, suggesting that Trem2 inhibits ambient but not LPS-dependent NFκB activity (fig. S12, C and D). We further examined MAPKs activation in BV2 cells using whole tumor cell antigen. We found dead SB28 cells did not activate microglial ERK and JNK but increased activation of NFκB and MAPK p38 in Trem2 knockdown BV2 cells compared to control cells (fig. S12, E and F). Therefore, Trem2 remodels microglial function by participating in multiple signaling pathways.

Given the antitumor effects of Trem2 loss-of-function macrophages and microglia using CM and the direct coculture system, we predicted that Trem2 loss-of-function myeloid cells could potentially kill tumor cells and inhibit tumor growth in vivo if present at the early stage of tumor initiation. We therefore designed an in vivo coimplantation model in which we inject SB28 GBM cells together with myeloid cells. We found that orthotopic coinjection of SB28 cells with control BV2 microglial cells did not alter animal survival compared to injection of tumor cells alone (Fig. 8D). However, coinjection of SB28 cells with Trem2 knockdown BV2 microglia significantly increased animal survival compared to injection of tumor cells with control cells (Fig. 8D). We found similar results with coinjection of SB28 cells with $Trem2^{-/-}$ BMDMs (Fig. 8E).

CORRECTED 24 MAY 2024; SEE ERRATUM

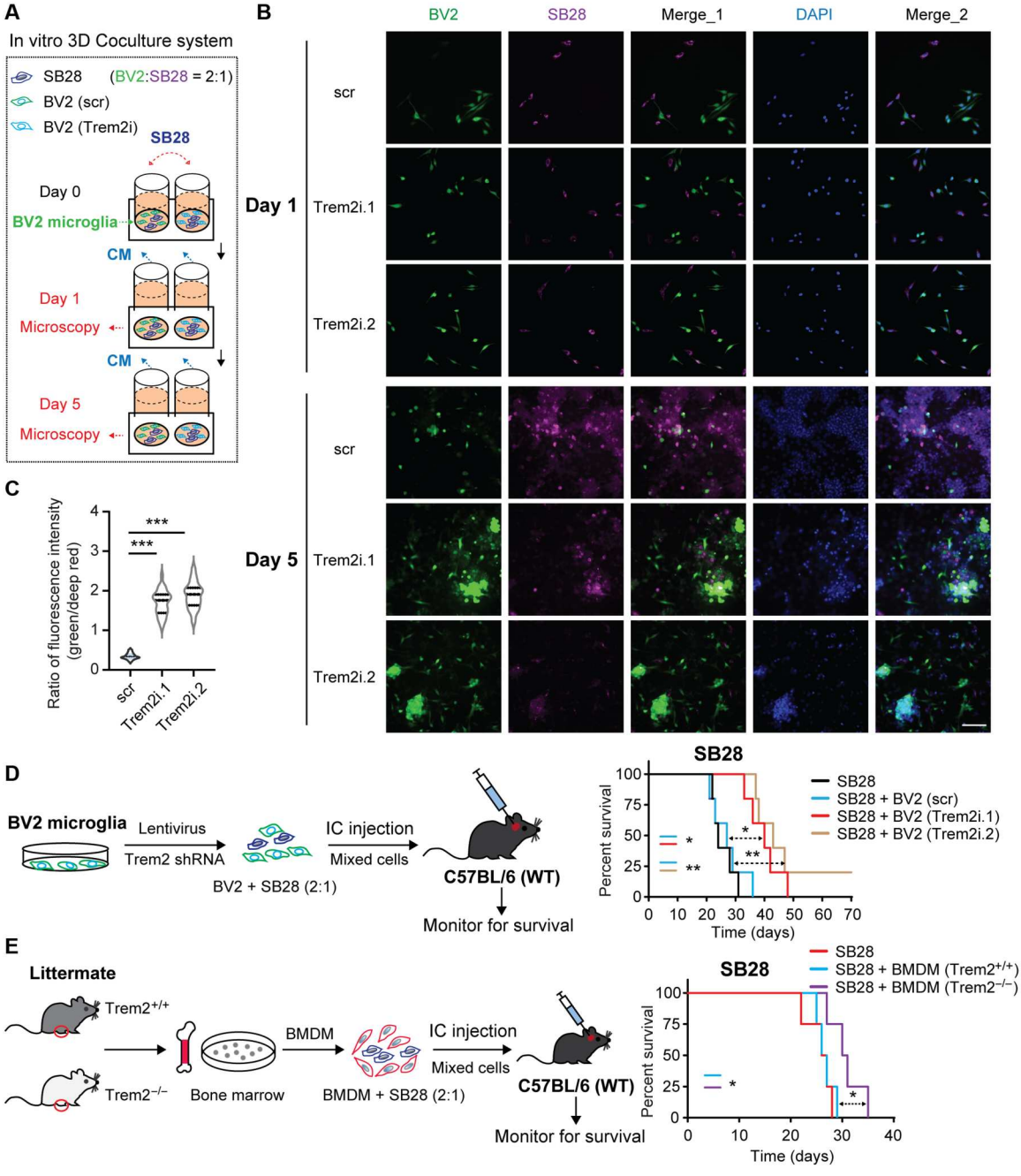

Fig. 8. Trem2 loss-of-function myeloid cells show antitumor effects both in vitro and in vivo. (**A** to **C**) Trem2 knockdown in BV2 microglia by Trem2-targeted shRNA lentivirus transduction (Trem2i.1 and Trem2i.2). Nonsilencing shRNA used as control (scr). BV2 and SB28 cells were stained with green and deep-red tracking dye, respectively, and cocultured in vitro. (A) Timeline schematic for treatment strategy. (B) Representative images. Green, BV2; purple, SB28; blue, nucleus (DAPI). Scale bar, 100 μm. (C) Violin plot indicating the ratio of mean fluorescent intensity (green/purple) at day 5 (quantified for 30 fields per condition). (**D**) GBM model of intracranial (IC) coimplantation of BV2 microglia and SB28 cells. Neurological deficit-free survival curves (right; $n = 5$ per group). WT, wild-type. (**E**) GBM model of BMDMs and SB28 coinjection. Neurological deficit-free survival curves (right; $n = 4$ per group). Data represent means ± SEM. $^*P < 0.05$; $^{**}P < 0.01$; $^{***}P < 0.001$.

Together, these results suggest that Trem2 loss-of-function myeloid cells have direct antitumor capacity in vivo.

Trem2 deficiency reprograms tumor-associated myeloid populations toward a proinflammatory phenotype

Our data indicate that Trem2-deficient myeloid cells exhibit enhanced antitumor activity and proinflammatory phenotypes in vitro and curb tumor growth in vivo using coinjection models. We next analyzed the phenotypes of tumor-associated myeloid

CORRECTED 24 MAY 2024; SEE ERRATUM

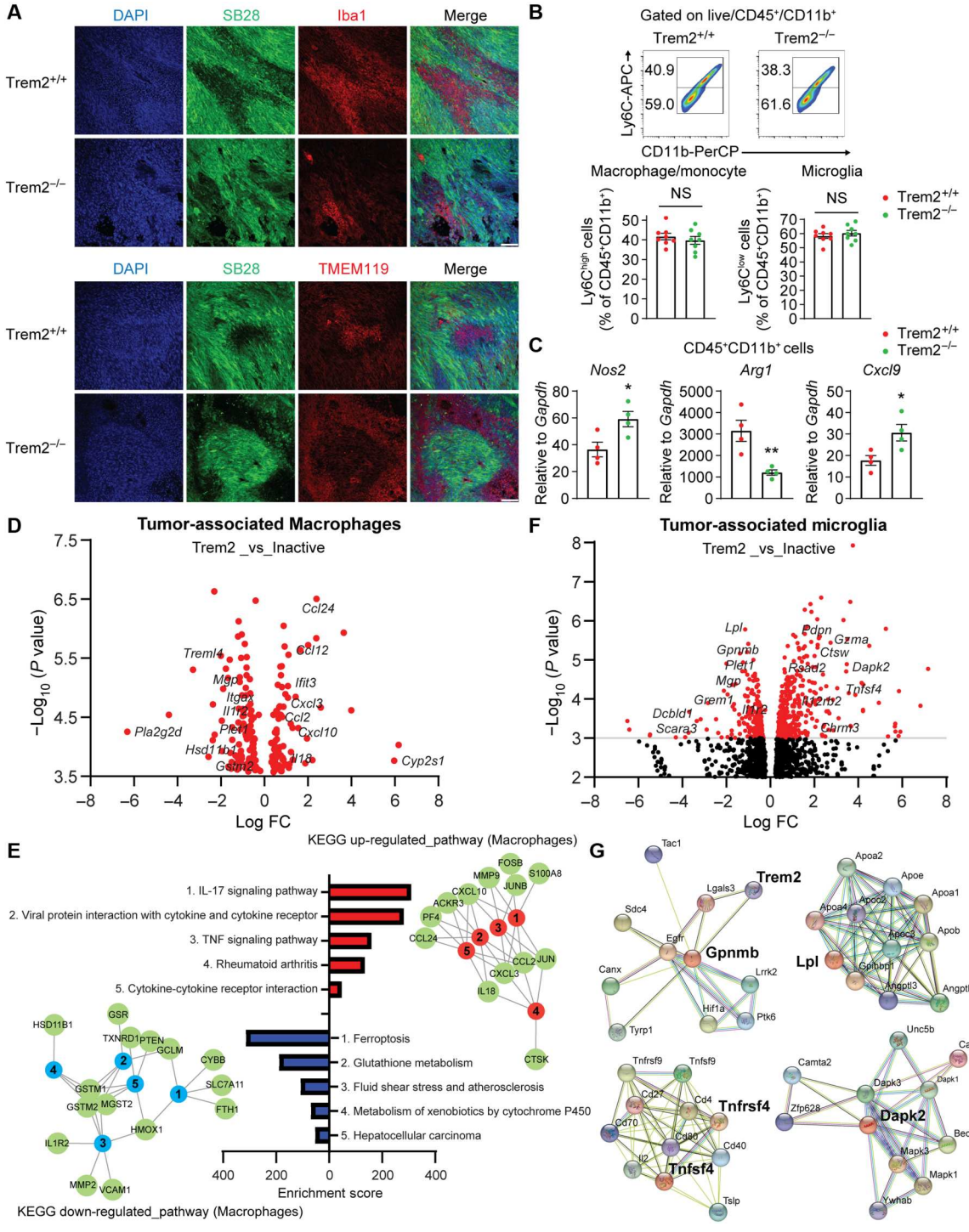

Fig. 9. Trem2 deficiency reprograms tumor-associated myeloid cells toward a proinflammatory phenotype. (**A**) Representative imaging showing that Iba1$^+$ and Tmem119$^+$ myeloid cell populations in SB28 tumor from *Trem2*$^{+/+}$ and *Trem2*$^{-/-}$ mice. Scale bars, 100 μm. (**B**) Representative pseudo-color/smooth plots showing intratumoral CD45$^+$CD11b$^+$ myeloid cells (top). Frequencies of Ly6C^{high} (macrophage/monocyte lineage) and Ly6C^{low} cells (resident microglia) among CD45$^+$CD11b$^+$ cell populations (bottom; n = 8/genotype). (**C**) Relative gene expression in tumor-associated CD45$^+$CD11b$^+$ myeloid cells from *Trem2*$^{+/+}$ and *Trem2*$^{-/-}$ mice (n = 4 per genotype). (**D** to **G**) *Trem2*$^{+/+}$ mice were intracerebroventricularly injected with Trem2-targeted ASO or inactive control. Then, ASO-treated mice were intracerebrally implanted with SB28 cells. Live CD45$^+$ cells isolated from brain tumors (day 30) and analyzed by scRNA-seq. (D) and (F) Volcano plots showing differentially expressed genes in macrophage subset (D) and microglia population (F) from Trem2 ASO–treated tumor versus from inactive ASO–treated tumor. (E) KEGG analysis of enriched up-regulated and down-regulated pathways in tumor-associated macrophage subset. Red, up-regulated; blue, down-regulated. (G) STRING protein interaction analysis of down-regulated genes (*Gpnmb* and *Lpl*) and up-regulated genes (*Tnfsf4* and *Dapk2*) in tumor-associated microglia from Trem2 ASO–treated tumor. Networks generated on STRING v11.5 (https://string-db.org/). Data represent means ± SEM. *P < 0.05; **P < 0.01. NS, no significance; FC, fold change.

cells in vivo in the context of Trem2 loss of function. We first examined the myeloid infiltrates of GBM tumors in *Trem2* transgenic mice. We found large numbers of Iba1$^+$ (pan-myeloid) and transmembrane protein 119 (TMEM119)$^+$ (microglial) myeloid infiltrates in SB28 orthotopic tumors in both *Trem2*$^{-/-}$ and *Trem2*$^{+/+}$ mice (Fig. 9A). No significant differences were observed in frequencies of both local and migrated myeloid subsets among total myeloid infiltrates between *Trem2*$^{+/+}$ and *Trem2*$^{-/-}$ mice (Fig. 9B). We then looked at inflammation-related gene expression (table S3) in intratumoral CD45$^+$CD11$^+$ cells that were sorted using flow cytometry (Fig. 9C). Expression of the typical proinflammatory genes *Nos2* and *Cxcl9* was higher in *Trem2*$^{-/-}$ myeloid infiltrates than in *Trem2*$^{+/+}$ myeloid infiltrates in tumors (Fig. 9C). In contrast, expression of the anti-inflammatory gene *Arg1* was higher in *Trem2*$^{+/+}$ myeloid infiltrates than in *Trem2*$^{-/-}$ infiltrates (Fig. 9C).

We then focused on the phenotypes of tumor-associated myeloid cells from Trem2 ASO-treated mice. Using scRNA-seq (fig. S13), we compared the differential gene expression of myeloid infiltrates between Trem2 ASO– and inactive ASO–treated mice (Fig. 9, D to G). For tumor-associated macrophages, we focused on the lipid metabolism–associated macrophage subset since we observed the most robust gene expression changes in Trem2 ASO–treated mice. We observed significantly up-regulated proinflammatory markers (*Ccl2*, *Ccl12*, *Cxcl3*, and *Cxcl10*), macrophage activation markers (*Il18* and *Cyp2s1*) (*55*), and IFN-induced protein (*Ifit3*) (Fig. 9D) (*56*). *Ccl24*, which mediates proinflammatory neutrophil and macrophage chemotaxis, was also increased in expression (Fig. 9D). Oppositely, genes that contribute to the resolution of inflammation and tissue repair (*57*) were significantly decreased in expression, such as *Mgp*, *Hsd11b1*, *Gstm2*, and *Plet1* (Fig. 9D). The expression of *Pla2g2d*, a M2-type macrophage marker (*58*), was also decreased (Fig. 9D). *Treml4*, a Trem family member that regulates inflammatory responses, decreased in expression as well (Fig. 9D). Furthermore, in Trem2 ASO–treated mice, this tumor-associated macrophage subset demonstrated significant up-regulation of the TNF and IL-17 signaling pathways (Fig. 9E), which are involved in tumor cell killing and proinflammatory responses. We also observed a decrease in ferroptosis pathway genes (Fig. 9E), which leads to lipid peroxidation and eventual cell death. In tumor-associated microglia of Trem2 ASO–treated mice, we observed a different set of up-regulated genes that contribute to a proinflammatory phenotype (Fig. 9, F and G): *Tnfsf4*, *Il12rb2*, and *Chrm3* are involved in proinflammatory response and cytokine induction; *Rsad2* is one of the most highly induced IFN effector genes; *Ctsw* and *Dapk2* (*59*) modulate lysosomal function and autophagy; *Gzma* and *Pdpn* play roles in phagocytosis and production of proinflammatory cytokines (*60*, *61*). As in tumor-associated macrophages, we observed decreased expression of *Mgp* and *Plet1* in the tumor-associated microglial subset of Trem2 ASO–treated mice (Fig. 9F). *Gpnmb* and *Grem1*, which inhibit macrophage M1 polarization (*62*, *63*), as well as *Lpl* and *Scara3* (*64*), which correlate with dysregulated lipid metabolism and anti-inflammatory responses, were down-regulated in microglia from Trem2 ASO–treated mice (Fig. 9, F and G). *Dcbld1*, associated with poor prognosis in patients with cancer (*65*), was also found to be down-regulated in tumor-associated microglia from Trem2 ASO–treated mice (Fig. 9F). Protein-protein network analyses (String) suggest that transmembrane glycoprotein NMB (Gpnmb) and Trem2 are functionally linked (Fig. 9G), tumor necrosis factor superfamily, member 4 (Tnfsf4) delivers costimulatory signals between microglia and T cells (Fig. 9G), and death-associated protein kinase 2 (Dapk2) regulates MAPK activity in microglia (Fig. 9G), implying that Trem2 regulates a wide range of intracellular and cell-cell signaling interactions. Together, tumor-associated myeloid cells in the setting of Trem2 loss of function demonstrate enhanced proinflammatory functions.

Trem2 deficiency increases PD-1$^+$CD8$^+$ T cells in the TME, and combined anti–PD-1 treatment improves animal survival

Trem2 loss of function reprograms the phenotypes and functions of myeloid infiltrates in the GBM TME. Given that cytotoxic T cells (CD8$^+$ T cells) are thought to represent a major immune subset that can kill tumor cells and inhibit tumor growth, we asked whether Trem2 deficiency affects T cell functions in GBM. T cells constitute a very small cellular fraction of the GBM TME, and suppressive myeloid cells use multiple mechanisms to inhibit T cell responses. We examined tumor-associated lymphoid infiltrates using ASO-treated mice bearing SB28 tumors. Trem2 ASO–treated mice demonstrated tumor infiltrates with higher frequencies of total T cells and CD8$^+$ T cells than control ASO–treated mice (Fig. 10A), implying a more robust T cell response in Trem2 ASO–treated mice. Moreover, Trem2 ASO–treated mice exhibited more T cells that express programmed cell death protein 1 (PD-1) in tumor infiltrates, especially CD8$^+$ T cells (Fig. 10A), suggesting increased T cell activation in the TME and potentially enhanced responsiveness to anti–PD-1 checkpoint blockade. We also examined PD-1 expression in CD8$^+$ T cells of tumor infiltrates from *Trem2* transgenic mice bearing SB28 tumors. Both the frequency of PD-1$^+$ T cells among CD8$^+$ T cells (Fig. 10B) and average PD-1 protein level in all CD8$^+$ T cells (Fig. 10C) were higher in tumors from *Trem2*$^{-/-}$ mice compared to *Trem2*$^{+/+}$ mice. Collectively, these results suggest that Trem2 deficiency remodels myeloid infiltrates in a manner that enhances T cell activation, likely contributing to restricted tumor growth in vivo.

Given these alterations in T cell number and phenotype, we then tested whether we could improve the efficacy of Trem2 deficiency in our tumor model with the addition of an immune checkpoint inhibitor, anti–PD-1 antibody (Fig. 10, D and E). We first tested the efficacy of anti–PD-1 immunotherapy in combination with *Trem2* transgenic mice in our tumor model (Fig. 10D). We found that compared to isotype treatment, anti–PD-1 administration significantly prolonged overall animal survival in SB28-bearing *Trem2*$^{-/-}$ mice despite initiating anti–PD-1 8 days following tumor injection (Fig. 10D). We also tested the ability of PD-1 in combination with Trem2 ASO treatment. It is known that the SB28 GBM model is completely resistant to anti–PD-1 treatment (*19*, *66*). Consistently, anti–PD-1 therapy (with control ASO) had no effect on animal survival in SB28-bearing mice (Fig. 10E). Compared to Trem2 ASO treatment alone, Trem2 ASO combined with anti–PD-1 treatment increased OS in SB28-bearing mice (Fig. 10E). Therefore, we conclude that TREM2 deficiency in the TME not only reprograms myeloid cell function but also promotes T cell infiltration and activation, which intensifies anti–PD-1 therapy (Fig. 10F). Together, Trem2 inhibition in myeloid infiltrates, including microglia and blood-lineage macrophages, reshapes the microenvironment toward a more immunologically "hot" status that suppresses GBM growth and leads to improved animal survival.

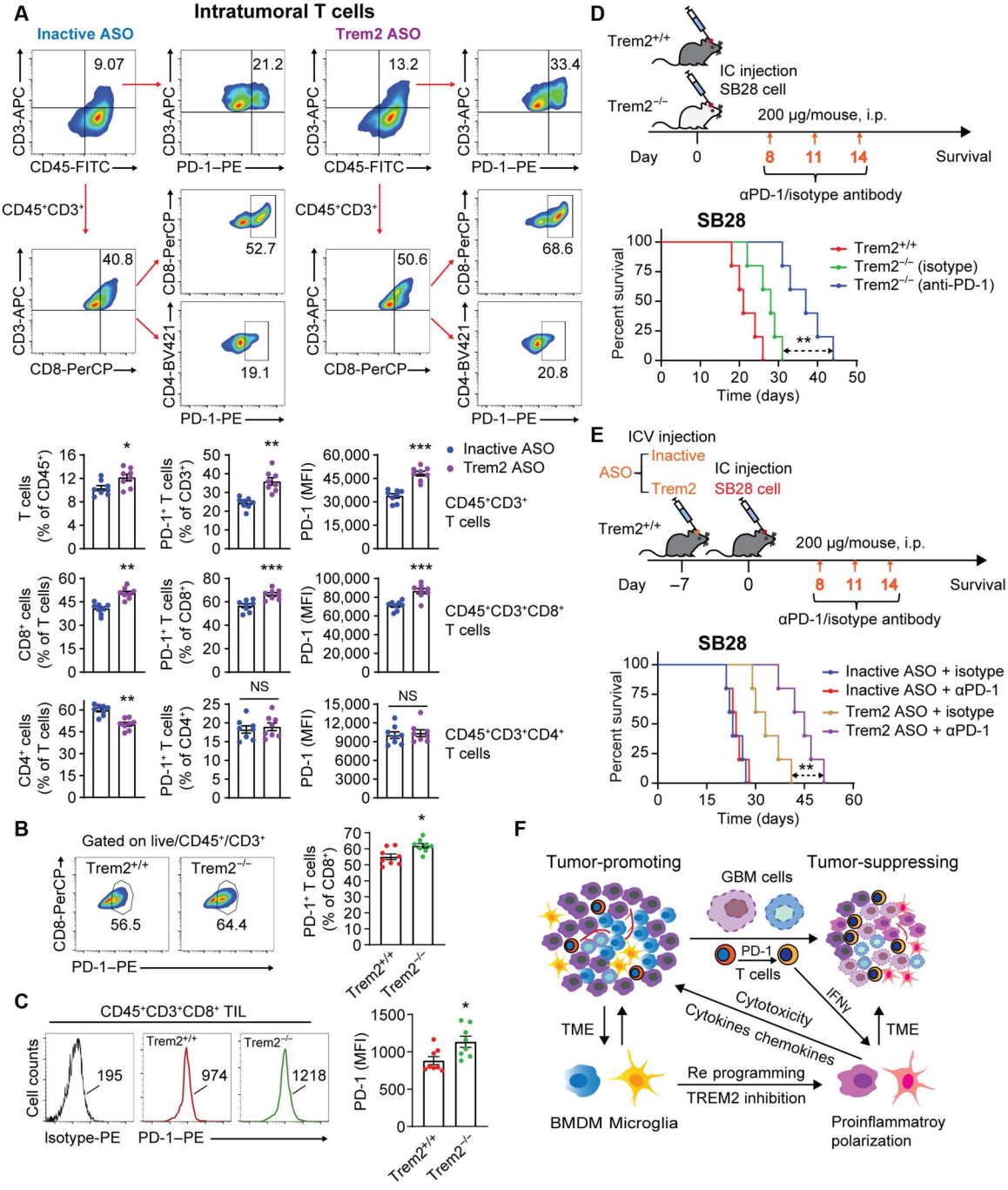

Fig. 10. Trem2 deficiency increases PD-1$^+$CD8$^+$ T cells in the TME, and combined anti–PD-1 therapy augments overall animal survival. (**A**) Representative pseudo-color/smooth plots showing intratumoral T cell subsets and PD-1 expression (top). Live CD45$^+$ cells isolated from SB28 tumors in ASO-treated mice and assessed by flow cytometry. Summary graphs showing frequencies of total T cells among CD45$^+$ cells, CD3$^+$CD8$^+$ and CD3$^+$CD4$^+$ subsets among T cells, and PD-1$^+$ cell among different T cell populations, and PD-1 protein levels [mean fluorescence intensity (MFI)] (bottom; $n = 8$ per condition). (**B** to **C**) Tumor-associated CD45$^+$ cells isolated from SB28-bearing *Trem2*$^{+/+}$ and *Trem2*$^{-/-}$ mice. PD-1 expression in CD3$^+$CD8$^+$ T cells was assessed by flow cytometry. (B) Frequency of PD-1$^+$ cells in CD3$^+$CD8$^+$ T cells. Representative flow plots (left) and summary graph (right; $n = 8$ per genotype). (C) PD-1 protein shown as MFI. Representative histograms (left) and summary graph (right; $n = 8$ per genotype). TIL, tumor-infiltrating lymphocyte. (**D** and **E**) Combined therapy in GBM. (D) Schematic (top). *Trem2*$^{-/-}$ mice were treated with anti–PD-1 antibody or isotype control following tumor implantation ($n = 5$ per condition). Symptom-free survival curves for SB28-bearing mice (bottom). (E) Schematic showing ASOs and anti–PD-1 treatment strategy (top). Neurological deficit-free survival curves for SB28 GBM model (bottom). (**F**) Schematic to describe Trem2 inhibition reshapes TME by modulating myeloid cell phenotypes and cytotoxic T cell function, which suppresses tumor progression. Data represent means ± SEM. *$P < 0.05$; **$P < 0.01$; ***$P < 0.001$. IC, intracranial; ICV, intracerebroventricular.

DISCUSSION

In this study, we identified that higher expression of TREM2 in *IDH1/2*–wild-type GBMs is associated with worse survival in patients with GBM and TREM2 expression is enriched in myeloid cell populations in GBM TME, including microglia and macrophage subsets. To explore the role of Trem2 in *IDH*–wild-type GBM, we used two syngeneic orthotopic mouse GBM models, SB28 (*22*) and NPA C54B (*24*). Using scRNA-seq and immunostaining, we found abundant Trem2^{+} myeloid infiltrates in the TME during GBM progression in vivo. We then used *Trem2* transgenic mice and found Trem2 loss of function in vivo leads to increased tumor cell apoptosis, slower tumor expansion, and improved animal survival in GBM-bearing mice. Previously, acute Trem2 reduction by anti-TREM2 antibody treatment was found to be more effective than TREM2 knockout in controlling tumor growth in a mouse sarcoma model (*15*). Considering the brain context of GBM, we further used ICV injection of Trem2-lowering ASOs to acutely knockdown Trem2 expression in mouse brain. We found that acute, brain-specific Trem2 reduction robustly reduced tumor size and increased animal survival in two GBM models. We corroborated this with anti-TREM2 antibody treatment, which also improved animal survival in GBM-bearing mice.

To understand the mechanism of Trem2 inhibition in regulating GBM progression, we focused on the Trem2-expressing populations in GBM TME, including blood-lineage macrophages and resident microglia. First, we found in vitro that IFNγ-induced *Trem2*$^{-/-}$ BMDMs demonstrated increased phagocytic and tumor-suppressing capacity than *Trem2*$^{+/+}$ BMDMs. Using bulk RNA-seq, we found that IFNγ-treated *Trem2*$^{-/-}$ BMDMs express a much higher level of M1-related, proinflammatory genes including *Tnf*, *Nos2*, *Ccl5*, and *Cxcl10*, which are highly enriched in TNF and NFκB signaling pathway, consistent with the increased tumoricidal activity of *Trem2*$^{-/-}$ BMDMs. We also stimulated BMDMs with tumor cell antigen to detect their antitumor responses. We found that upon both IFNγ and tumor antigen treatment, *Trem2*$^{-/-}$ BMDMs were more immunoactive by expressing higher levels of activated myeloid cell markers such as *Cd80*, *Cd83*, *H2-T24*, and *Nampt* and lower levels of chemokine receptors related with immune tolerance, such as *Ccr1* and *Ccr5*. Moreover, *Trem2*$^{-/-}$ BMDMs showed much higher expression of genes related with endosomal/lysosomal functions, such as *Npc1*, *Ctsd*, *Ctsz*, *Atp6v1a*, *Lamp1*, and *Lamtor3*, contributing to intracellular antigen processing and presentation. Lipid uptake and metabolism, associated with anti-inflammatory phenotypes in myeloid cells, were significantly down-regulated in *Trem2*$^{-/-}$ BMDMs. In addition, we found that TREM2 knockdown human macrophages exhibited more cytotoxic effects on human GSCs than control macrophages. In human macrophages, TREM2 was also found to restrict IFNγ-induced immunoactivation and proinflammatory phenotypes. We identified TNFα as one of the secreted antitumor factors in TREM2 knockdown human macrophages and provide evidence for additional secreted antitumor proteins, which remain to be found. Moreover, TREM2 knockdown restrained human macrophage M2 polarization. Together, TREM2 inhibition can remodel macrophages toward an immunoactive functional state in vitro.

Our results using BM chimeric *Trem2* transgenic mice in the SB28 GBM model revealed that Trem2 loss of function in brain microglia also played an important role in tumor suppression in vivo. We further examined how Trem2 regulates microglial function by using the BV2 cell line (*44*) and primary microglia (*45*). We found that Trem2 loss of function in both BV2 cells and primary microglia boosted phagocytic capacity. Both Trem2 knockdown BV2 cells and Trem2 ASO–treated primary microglia showed augmented tumor–suppressing function. Gene expression profiling of primary microglia upon IFNγ or tumor antigen stimulation revealed that Trem2 inhibition significantly inhibited the expression of genes that down-regulate inflammation or promote immunosuppression, such as *Gsn*, *Clec7a*, *Plcg2*, *Cd44*, *Cd33*, *Plau*, and *Ccl9*, and highly induced the expression of genes involved in antigen presentation, cytokine induction, or proinflammatory phenotypes, including *H2-D1*, *Ctsz*, *Npc2*, *Atf4*, *Sqstm1*, and *Mcl1*. Thus, Trem2 inhibition promotes immunoactive microglial differentiation.

To further validate that Trem2 inhibition enhances antitumor activities in both macrophages and microglia, we performed direct coculture of myeloid and GBM cells in vitro and a coimplantation model using primary BMDMs or BV2 cells with GBM cells in vivo. We found, both in vitro and in vivo, that Trem2 loss-of-function myeloid cells demonstrate tumor-suppressing function. These data indicate that Trem2 loss of function in the TME inhibits tumor growth and further suggests that myeloid phenotypes rather than the absolute number of myeloid cell populations in the TME affect tumor growth.

To expand our knowledge of how Trem2 regulates classical signaling of myeloid cells, we used the BV2 model. We found that Trem2 was involved in multiple signaling pathways in BV2 cells. Trem2 knockdown decreased STAT1 overactivation upon IFNγ treatment, which may prevent sustained expression of apoptosis-related ISGs and lead to increased microglial survival (*67*, *68*). Moreover, Trem2 knockdown remodeled LPS-induced activation of MAPKs signaling, including decreased ERK and JNK activation and increased MAPK p38 activation. Essential roles for the MAPKs in macrophage function have been established: ERK signaling contributes to the M2-type macrophage development and anti-inflammatory cytokine induction (*69*, *70*); Activation of JNK family members is important for M1 polarization and macrophage survival (*71*); MAPK p38 pathway is activated in M1 macrophages and supports cell survival as well as the production of proinflammatory mediators, such as TNFα (*70*, *72*). In this regard, we found that activation of MAPK p38 correlates with enhanced proinflammatory response in Trem2 knockdown BV2 cells. Moreover, Trem2 knockdown elevated NFκB activation at baseline, which may, in part, explain why CM from Trem2 knockdown cells more potently inhibit the proliferation of GBM cells. We examined MAPK activation in BV2 cells that have been stimulated with dead tumor cells. In this context, we did not observe activation of ERK and JNK in both control and Trem2 knockdown microglia. However, Trem2 knockdown BV2 cells exhibited significantly increased NFκB and MAPK p38 activation, both of which induce genes that inhibit cell apoptosis and enhance inflammation (*73*).

Considering the complexity of GBM TME, we further investigated the phenotypes of tumor-associated myeloid cells in vivo by flow cytometry and scRNA-seq. We found tumor-associated *Trem2*$^{-/-}$ myeloid cells more highly express the M1-phenotype genes and more lowly express the anti-inflammatory gene *Arg1*. Using acute Trem2 knockdown GBM model, we found that proinflammatory molecules including Ccl2, Ccl12, Cxcl3, and Cxcl10 and the TNF signaling pathway are significantly up-regulated in Trem2-inhibited

in the lipid metabolism-associated macrophage subset, in line with what we have observed in vitro. Tumor-associated microglia with Trem2 reduction demonstrated increased lysosomal function and autophagy (*Ctsw* and *Dapk2*), consistent with our in vitro results using cultured primary microglia (*Ctsz* and *Npc2*). Moreover, the expression of genes (*Tnfsf4*, *Il12rb2*, *Pdpn*, and *Chrm3*) that promote proinflammatory response and cytokine induction were increased tumor-associated microglia in the context of Trem2 deficiency. On the contrary, we observed that the gene expression profiles that contribute to anti-inflammatory responses and tissue homeostasis were down-regulated in both Trem2-inhibited tumor-associated macrophages and microglia. For example, *Mgp* and *Plet1* expression was decreased in both the macrophage subset and microglia. Overall, tumor-associated myeloid cells with Trem2 loss of function demonstrated enhanced proinflammatory functions, corroborating our in vitro findings.

Furthermore, we found molecules that play roles in lipid uptake and metabolism were significantly inhibited in expression in Trem2 loss-of-function myeloid cells (macrophage and microglia) both in vitro and in vivo, such as Cd36, LPL, phospholipase A2 group IID (PLA2G2D), PLCG2, Treml4, and scavenger receptor class A member 3 (SCARA3). It has been reported that TREM2 is a lipid-binding cell surface receptor and TREM2 drives the generation of lipid-associated macrophages (LAMs), which regulate lipid metabolism through the expression of genes such as *Cd36*, *Lpl*, *Fabp4*, *Fabp5*, among others (*74*, *75*). TREM2$^+$ LAMs display M2 macrophage phenotypes and maintain tissue homeostasis (*74*–*76*). In breast cancer, the TREM2$^+$ LAM subpopulation has been identified to support an immunosuppressive microenvironment, and genetic depletion of this LAM subset in mice suppressed tumor growth (*77*). We speculate Trem2 loss of function in vivo may play a particularly important role in reprogramming LAM function in the GBM TME to augment the antitumor response.

Previous reports have found that TREM2 inhibition slows the growth of mouse sarcoma and subcutaneous tumor, with increased response to anti–PD-1 treatment (*14*, *15*). We examined the T cell populations in GBM-bearing mice and found that both Trem2 knockout and Trem2 ASO treatment resulted in increased PD-1$^+$CD8$^+$ T cell numbers in GBM TME. We then tested the combined effect of Trem2 loss of function and anti–PD-1 treatment for GBM therapy and found that anti–PD-1 further enhanced the therapeutic efficacy of Trem2 inhibition in tumor-bearing animals. We thus conclude that Trem2 inhibition contributes to tumor suppression in vivo by reshaping myeloid subset and T cell functions and that Trem2 inhibitory strategies, especially in combination with immune checkpoint blockade, may represent an attractive new approach for GBM therapy. Whether Trem2 regulates the phenotypes of other immune cell subsets to provide potentially additional therapeutic opportunities remains an open question for future studies.

MATERIALS AND METHODS

Study design

The objective of this study was to determine the role of TREM2 in GBM tumor cell growth and evaluate whether TREM2 inhibition is of value for GBM therapy using both primary human GBM cells and mouse models of GBM. For in vitro experiments, samples were randomly selected for treatment, and both data collection and analysis were performed in a blind fashion in regard to treatment group. For in vivo experiments, mice were randomly assigned to treatment groups with littermate controls or otherwise relevant controls (control knockdown or knockout myeloid cells, control ASO treatment). Investigators were blinded to mouse genotype or group before treatments. No data were excluded from the analysis. Primary GBM cell cultures were generated from fresh GBM tumor tissue obtained from Barnes-Jewish Hospital/Washington University School of Medicine. Experiments with human tumor tissue were conducted in accordance with approved institutional review board protocols: IRB# 201211019, 201409046. Informed consent was obtained per protocol from patients before usage. Experiments with animals were conducted in accordance with approved institutional review board protocols (#21-0083) and adhere to National Institutes of Health and American Association for Laboratory Animal Science guidelines and have been approved by our Institutional Animal Care and Use Committee (IACUC).

Plasmids preparation and lentiviral production

All human and mouse gene target-directed short hairpin–mediated RNA (shRNA) clones in this study were purchased as bacterial glycerol stock, and amplificated shRNA plasmids were isolated through QIAprep Spin Miniprep and EndoFree Plasmid Maxi kits (QIAGEN) per instructions. Two human TREM2 gene RNAi with corresponding scrambled RNAi were selected as follows: TREM2i.1 (TRCN0000056719), scr.1 (SHC002) (Sigma-Aldrich), TREM2i.2 (RHS4430-200284823), and scr.2 (RHS4346) (GIPZ Lentiviral shRNA, Horizon Discovery). Mouse Trem2 gene RNAi with high knockdown efficiency were used: Trem2i.1 (TRCN0000068096) and Trem2i.2 (TRCN0000068097) (Sigma-Aldrich); and SHC002 was the nontargeting control. In this study all shRNA clones are listed as table S1.

Human embryonic kidney 293T cells were used for shRNA-expressing lentiviral packaging. Briefly, HEK 293T cells were seeded into six-well plates one day before plasmids transfection. With cell confluence arriving at 70 to 80%, transfection was performed by making DNA/PEI (Polysciences) complexes into Opti-MEM medium (Gibco). The shRNA plasmid was mixed with packaging plasmid psPAX2 and envelope plasmid pCMV-VSVG by a ratio per instructions. On day 6, culture medium was collected, centrifuged for dead cell debris removal, and filtered through 0.45-μm syringe filter. Lenti-X Concentrator (Clontech) was then used to concentrate lentivirus in the supernatant. After incubation at 4°C for 6 to 7 hours, virus-containing pellets were collected by centrifuging at 1500*g* for 45 min at 4°C, resuspended in cold phosphate-buffered saline (PBS), and stored at −80°C in single-use aliquots.

Syngeneic orthotopic tumor implantation

Two mouse syngeneic GBM models were used in this study. A total of 10,000 cells injection per animal was performed for a slow SB28 tumor developing model. A total of 2000 cells injection per animal was used for developing NPA C54B glioma in vivo. For a coimplantation model, SB28 tumor cells and primary BMDMs or BV2 cells, by a number ratio of 1:2, were mixed and coinjected into the mouse brain. Cells were stereotactically (David Kopf Instruments) injected into the right putamen of age-matched *trem2* transgenic mice or 6 to 8 weeks old C57BL/6 mice. The coordinates used were as follows: 1.0 mm rostral to bregma, 1.5 mm lateral, and 2.0 mm deep. Mice's

survival was monitored and euthanized on the basis of neurological-deficient symptoms according to IACUC guidelines.

ASO design and ICV injection

Trem2-targeted and inactive ASOs were designed as reported (*25*) and synthesized (Integrated DNA Technologies). The knockdown effects of Trem2-lowering ASO at different concentrations were evaluated in BV2 cells in vitro (*25*). In vivo injection was performed as described (*25*). Briefly, Trem2-targeted and inactive ASOs were diluted in sterile saline and administered via ICV injection. Seven days later, mice were stereotactically injected with GBM cells as mentioned above. Mice′s survival was monitored and euthanized on the basis of neurological-deficient symptoms.

In vivo treatments

After tumor implantation, *trem2* transgenic mice were treated with sotuletinib (BLZ945, brain-penetrant CSF-1R inhibitor) or vehicle (20% Captisol) [MedChemExpress (MCE)]. Mice were dosed with sotuletinib (200 mg/kg) or vehicle by oral gavage at days 7, 12, and 17. Symptom-free survival was evaluated. Mice were treated intraperitoneally with anti-TREM2 antibody (clone 178; 200 μg per mouse) or isotype control (clone 135) at days 4, 8, 12, and 16 after tumor injection. Mice were intraperitoneally injected with anti–PD-1 antibody (200 μg per mouse, BioXCell) or isotype control (rat IgG2a) at days 8, 11, and 14 after tumor injection.

Generation and culture of mouse BMDMs

The isolation and differentiation of mouse BMDMs by macrophage colony-stimulating factor (M-CSF) have been performed (*26*). Briefly, mice between 6 and 12 weeks of age were euthanized following IACUC guidelines. The lower limb was exposed by removing the skin. The femur and tibia were collected by cutting off the base of femur into the spine and Achilles tendon round tibia. Major muscles and fibula were then removed. After removing the epiphyses of femur and tibia, BM cells were washed out by sterile PBS using 23-gauge needles. Cell pellets were collected by centrifuging at 500*g* for 5 min at 4°C and resuspended with 10 ml of Dulbecco′s modified Eagle′s medium (DMEM) supplemented with 10% fetal bovine serum (FBS) and 1% penicillin-streptomycin. Cells were filtered through a 70-μm cell strainer and centrifuged again. After a gentle pipetting in complete DMEM with M-CSF (10 ng/ml), cells were seeded into 10-cm-diameter polystyrene-treated tissue culture dishes for a 7-day continuous differentiation. On day 3, half volume of culture medium was replaced with fresh M-CSF–containing DMEM. On day 7, cell morphology was assessed, and medium was changed without M-CSF. BMDM was then prepared for both in vitro stimulation and in vivo injection experiments.

Primary microglia culture

Primary microglia were isolated according to the published method (*45*) with modification. Briefly, primary cortical glial cultures were generated from postnatal day 2 mouse pups and cultured in DMEM supplemented with 10% FBS. After 2 to 5 days, the media were replaced with fresh DMEM containing granulocyte M-CSF (2 ng/ml). Once the microglia were blooming, they can be purified by agitation on an orbital shaker at 200 rpm for 2 hours at 37°C. Cell pellets were collected by centrifugation at 440*g* for 5 min, resuspended in a 1:1 ratio of fresh astrocyte culture media/old media, and seeded into 24/96-well plates. The next day, the media were replaced with microglia treatment media supplemented with 0.1% bovine serum albumin (BSA) and M-CSF (10 ng/ml). Microglia from *trem2* transgenic mice were assayed for phagocytotic activity or directly cocultured with GBM cells. Primary microglia (C57BL/6 background) were treated with 10 μM inactive ASO controls or Trem2-targeted ASO.

Phagocytosis assay

The phagocytotic capacity of BMDMs and primary microglia from *trem2* transgenic mice and BV2 cells with Trem2 knockdown was detected using Fluoresbrite YG Microspheres (Polysciences). Cytochalasin D (Sigma-Aldrich) was used as the negative control and added into wells 1 hour before microsphere treatment. Cells were incubated with YG beads (1:2000 dilution in medium) for 2 hours at 37°C. The medium was then removed, and cells were washed three times with 1× PBS. Cells were fixed with 4% paraformaldehyde (PFA; ProSciTech) at 4°C for 15 min and stained with 4ith stained t 4 (with 4% pa (DAPI) (1:5000 dilution in PBS). Primary microglia were labeled with Iba1 (GeneTex) primary antibody overnight, followed by incubation in Alexa Fluor 568–conjugated goat anti-mouse secondary antibody (1:500 dilution; Invitrogen) for 2 hours at room temperature. Images were captured on a microscope (Leica Microsystems). Bead colocalization with cells was quantified by ImageJ colocalization plugin and cell count (DAPI).

Flow cytometry

SB28 GBM-bearing mouse was euthanized following IACUC guidelines, and the brain tumor was dissected. Tumor tissues were dissociated to generate single-cell suspensions using a Brain Tumor Dissociation Kit (Miltenyi Biotec) according to the manufacturer′s instructions. Cell numbers were counted and incubated with CD45 MicroBeads (Miltenyi Biotec) for 15 min at 4°C. Live $CD45^+$ cell fractions were enriched by running cell suspensions through MACS Columns in a Magnetic MACS Separator (Miltenyi Biotec). $CD45^+CD11b^+$ cell fractions were then enriched using CD11b MicroBeads (Miltenyi Biotec). Two antibody panels were used for flow cytometry analysis: the myeloid TME composition, anti-mouse fluorescein isothiocyanate (FITC)–CD45 (1:200), allophycocyanin (APC)-Ly6C (1:100), PerCP-CD11b (1:100) (BioLegend), and phycoerythrin (PE) donkey anti-rabbit immunoglobulin G (IgG) (1:200; BioLegend) and Trem2 polyclonal antibody (1:100; Bioss); the lymphoid TME component, anti-mouse APC-CD3 (1:50), PerCP-CD8 (1:100), and PE-CD279 (PD-1) (1:20) (BioLegend). Briefly, cells were incubated with TruStain FcX-Fc blocker CD16/32 (BioLegend) for 15 min at room temperature. Then, cells were stained with different panels of antibodies or isotype controls. Samples were read on LSRFortessa (BD) and analyzed using FlowJo_v10.8.1 software.

Hematoxylin and eosin staining

Mouse brain with tumor implantation was fixed by 4% PFA (ProSciTech) perfusion and embedded into optimal cutting temperature (OCT) (Sakura) blocks. Frozen OCT tissue blocks were sectioned into 30 μm in thickness using cryostat (Leica Biosystems) and preserved at −20°C. Frozen sections were rehydrated in 100, 90, and 70% ethanol solution sequentially for 2 min at each. Tissue nuclei was stained by immersing sections in Gill Hematoxylin 2 (Thermo Fisher Scientific) for 3 to 4 min. Sections were then washed in double-distilled H_2O and dipped into Bluing agent (Agilent) for

30 s to complete the nuclear staining. After 20 dips in 95% ethanol, tissue slides were immersed in eosin (Agilent) for 1 min to get cytoplasm counterstain. With one dip of water wash, slides went through dehydration process by two times of 30 dips in 95% ethanol solution and two 5-min washes in 100% ethanol. Slide tissues were mounted with Cytoseal 60 (Thermo Fisher Scientific) for long-term storage at room temperature.

Immunohistochemistry

SB28 cells were stained with tracking dye: Cytopainter (green fluorescence) (Abcam) based on the manufacturer′s instructions. Then, cells were stereotactically (David Kopf Instruments) injected into the right putamen of C57BL/6 mice. Mouse was euthanized when neurological-deficient symptoms develop. Brains were dissected and embedded into OCT medium. Frozen OCT tissue blocks were sectioned into 30 μm in thickness and blocked with 10% normal goat serum (Vector Laboratories) in PBST (PBS containing 0.1% Triton X-100) for 1 hour at room temperature. Sections were incubated with Iba1 (GeneTex), TMEM119 (ABclonal), or cleaved caspase-3 (Cell Signaling Technology) primary antibody overnight at 4°C. After three washes in PBST, tissues were applied with Alexa Fluor 568/488–conjugated goat anti-mouse/rabbit IgG (H + L) secondary antibody (Invitrogen) for 2 hours at room temperature. With additional washes, sections were mounted with Fluoromount-G containing DAPI (Southern Biotech). Images were taken on a microscope (Leica Microsystems).

Conditioned medium

Different CMs were collected for study: THP-1 macrophage-like cells were cultured for 48 or 72 hours, as well as under IFNγ (20 ng/ml), LPS (10 ng/ml), or IL-4 and IL-13 (20 ng/ml) treatment for 24 or 48 hours, respectively; THP-1–derived macrophages were cultured with control IgG1/anti-TNFα antibody (10 ng/ml; adalimumab, MCE) for 48 hours; BMDMs and primary microglia treated with ASOs were cultured for 48 or 72 hours or stimulated with IFNγ (10 ng/ml) for 24 or 48 hours, respectively; BV2 microglia were cultured for 48 or 96 hours with/without IFNγ (50 ng/ml) treatment; BV2 microglia and SB28 cells were cocultured by a direct-contact manner. Aliquot CM was stored at −20°C. For cytotoxicity assays, CM was added into target cells′ medium, and the ratio of medium volume was 1:4.

Cytotoxicity assay

The cytotoxic effects on GBM cells were assessed by cell viability/proliferation assays in this study. To measure the effects of CM from human THP-1–derived macrophages on human GSCs, adenosine 5′-triphosphate (ATP) generation by viable cells was detected using CellTiter-Glo luminescence cell viability assay (Promega) per the manufacturer′s instructions, and YOYO-1 (Invitrogen) staining on dead cells was evaluated. 3-(4,5-dimethylthiazol-2-yl)-5-(3-carboxymethoxyphenyl)-2-(4-sulfophenyl)-2H-tetrazolium (MTS) colorimetric reagent (Promega) was also used to determine the number of viable cells by measuring absorbance at 490-nm wavelength. Absolute cell counting and ATP assays were performed to examine cell viability/proliferation of SB28 cells when cocultured with BMDMs or BV2 microglia in a Transwell system (Corning).

Enzyme-linked immunosorbent assay

Tumor necrosis factor (TNFα) secretion in the supernatants was assayed by ELISA (enzyme-linked immunosorbent assay) MAX Standard Set Mouse TNF-α kit (BioLegend) per the manufacturer′s instructions.

Nitrite assays (Griess)

The NO level in cultured supernatants was measured by modified Griess reagent (Sigma-Aldrich). Briefly, 150 μl of supernatant per sample was mixed with equal volume of 1× Griess reagent in a 96-well microplate. After 15-min incubation at room temperature, the NO concentration (nitrite) was determined by measuring the absorbance at 540 nm on the Cytation 5 multimode reader (BioTek).

In vitro three-dimensional coculture system

The direct interaction between microglia and GBM cells was assessed by three-dimensional (3D) coculture system in vitro. Briefly, primary microglia or BV2 cells and GBM cells were labeled with tracking dyes respectively: primary microglia/BV2 cells and Cytopainter (green fluorescence); GBM cells and Cytopainter (deep red fluorescence) (Abcam) based on the manufacturer′s instructions. Microglia and tumor cells were mixed at the ratio of 2:1 and added into the chamber slide (Thermo Fisher Scientific) in complete medium to support the growth of two cell types. Chambers were removed on days 1, 3 and 5, and cells on slide were fixed with 4% PFA (ProSciTech) for 15 min on ice. Slides were mounted with DAPI-containing medium. The supernatants on days 1, 3 and 5 were collected and assayed for cytokines. Cells on slides were observed on a microscope (Leica Microsystems), and fluorescence intensity was quantified using ImageJ.

RNA isolation and RT-qPCR

Cells were washed with ice-cold PBS and processed for total RNA isolation using QIAshredder and RNeasy Plus Mini Kit (QIAGEN) according to the manufacturer′s instructions. RNA was then reversely transcribed into cDNA by a High-Capacity cDNA Reverse Transcription Kit with RNase Inhibitor (Applied Biosystems). RT-qPCR was performed by using Power SYBR Green PCR Master Mix (Applied Biosystems) on CFX Connect Real-Time PCR Detection System (Bio-Rad) with a reaction setup as below: initial cycle, 95°C for 10 min; amplification stage, 40 cycles involving a denaturing step (95°C for 15 s), an annealing step (57°C for 30 s), and extension step (72°C for 30 s); a melting curve analysis, 65°C for 5 s and then 5 s each at 0.5°C increments between 65° and 95°C. Glyceraldehyde-3-phosphate dehydrogenase (GAPDH) was used as the internal reference gene and analysis is conducted on CFX Manager software (Bio-Rad) and Excel 2015 (Microsoft). Sequences for each pair of primers were listed in tables S2 and S3.

Western blot

Protein levels of trem2 gene expression in primary microglia, BV2 and THP-1 cell samples were confirmed by Western blot. To assess phosphorylated states of proteins under different stimuli in primary microglia and BV2 cells, Western blot assays were performed as below: Primary microglia were treated with IFNγ (10 ng/ml) for 30 min or dead SB28 cells for 60 min; BV2 cells were treated with IFNγ (10 ng/ml) or LPS (100 ng/ml) for 30 and 60 min, respectively, or dead SB28 cells for 90 and 120 min. Quickly, cell samples per

time point were washed three times with cold PBS and lysed on ice for 30 min in 1× radioimmunoprecipitation assay buffer (Cell Signaling Technology) with Protease Inhibitor Cocktail (MilliporeSigma). The lysates were then centrifuged at 15,000*g* for 20 min at 4°C. The supernatants were collected, and concentrations were determined using Protein Assay Dye Reagent (Bio-Rad) per protocol. Proteins each sample were then separated on 10 or 12% SDS–polyacrylamide gels and transferred onto 0.45-μm polyvinylidene difluoride membranes (Millipore). After 1 hour of shaking in blocking buffer (3% nonfat milk or BSA in PBS containing 0.05% Tween 20) at room temperature, membranes were incubated with primary antibodies overnight at 4°C. Next day followed by three washes using PBST buffer (PBS with 0.05% Tween 20) for 5 min per each, the membrane was incubated with IRDye 800CW donkey anti-rabbit IgG or IRDye 680RD donkey anti-mouse IgG secondary antibody (LI-COR Biosciences) (1:10,000 dilution in PBST buffer containing 1% BSA) for 2 hours at room temperature. After four washes in PBST buffer, blots on membranes were detected on Odyssey Fc Imaging System (LI-COR Biosciences). Primary antibodies used in this study include the following: TREM2 (Proteintech); phospho-STAT1, phospho-ERK, phospho-JNK, phospho-IκBα-S32, STAT1, ERK1/ERK2, JNK, IκBα, TREM2, Bcl-2, and Bax (ABclonal); TREM-2 (B-3) and GAPDH (6C5) (Santa Cruz Biotechnology); phospho-p38 MAPK (D3F9) and p38 MAPK (D13E1) (Cell Signaling Technology).

Bulk RNA-seq and data analysis

Primary myeloid cell populations were collected for transcriptomic analysis. BMDMs from *trem2* transgenic mice were treated with IFNγ (10 ng/ml), LPS (100 ng/ml), or dead SB28 cells for 6 hours. Primary microglia from nontransgenic mice were treated with ASOs for 3 days and then stimulated with IFNγ (10 ng/ml) or dead SB28 cells for 6 hours. Total RNA per sample was isolated using RNeasy Plus Mini Kit (QIAGEN) according to the manufacturer's instructions. RNA samples were submitted to the McDonnell Genome Institute (Saint Louis, MO) for mRNA-seq library generation and sequencing (Illumina NovoSeq). Generated data were then analyzed according to the published method (*78*). Differentially expressed genes ($P_{adj} < 0.05$) were clustered using *k*-means clustering and heatmaps of *z*-scores generated using Phantasus. Pathway analysis for each cluster was performed using EnrichR-KG using the KEGG database.

3′ scRNA-seq and data processing

Dissociated single-cell suspensions from human GBM samples (B150 and B152) or SB28 tumors (nontransgenic mice) were processed using the 10x Genomics Chromium Controller and the Chromium Single-Cell 3 oceLibrary & Gel Bead Kit following the manufacturer's protocols (https://tinyurl.com/ybpg2pfz). The yielded cDNA libraries were sequenced on an Illumina NovaSeq platform. All samples were processed using an in-house Workflow Description Language (WDL) pipeline. The pipeline first makes doublet predictions on raw 10x data using DoubletCollection wrapper, in which six doublet callers are used including "cxds," "bcds," "hybrid," "scDblFinder," "DoubletFinder," and "doubletCells." Doublet rate of 0.08 was used for calling these doublets. Data were further processed using Seurat version 4.0.0. Cells were filtered on the basis of nFeature > 700 (number of genes detected in each cell), nCount [unique molecular identifier (UMI) count] > 93rd percentile, and percent.mito > 0.05 (percentage of mitochondrial genes). Merged SB28 samples were clustered and projected on the UMAP using 50 principal components and a clustering resolution of 1.2. Cell types for clusters were predicted using Sctype. Both immune and brain cell markers were used in the prediction. Trem2 expressions across different cell clusters were ranked. Data for human GBM tumors were processed using our WDL pipeline as described. Cell type predictions were made using our in-house GBM cell type calling pipeline. Cells were first divided into $CD45^+$ and $CD45^-$ clusters. SingleR (version 1.4.1) was used for reference-based cell type identification. For the $CD45^+$ subset, Brain Immune Atlas (*56*) and STAB data (*79*) were used as reference datasets for cell type prediction. For the $CD45^-$ subset, reference datasets included previously published (*18*) and STAB data (*79*). Cell types less than 1% abundance in clusters were filtered out. TREM2 expression in different cell clusters was ranked and plotted.

Tumor tissues from ASO-injected mice were dissected and dissociated into single-cell suspensions. Live $CD45^+$ cell fractions were enriched through magnetic sorting. Mixed $CD45^+$ and $CD45^-$ cell suspensions were submitted to the McDonnell Genome Institute (Saint Louis, MO) for 10x Genomics library preparation and sequencing. Unfiltered gene expression matrices were processed using SoupX to reduce ambient reads in each sample. Datasets were then further processed using Seurat v4.0. Cells were filtered to remove cells with % mt-reads > 5% and total genes < 300 and > 9000 per cell. Data were then normalized using sctransform package with % mt-reads regressed and datasets integrated. Principal components analysis was performed and the first 20 dimensions were used in the FindNeighbors and RunUMAP commands in Seurat. Clusters were identified over a range of resolutions from 0.2 to 1.0. Two low-quality cell clusters determined by low numbers of genes and counts and coexpression of multiple cell type–specific markers were removed, as were two small clusters pertaining to astrocytes and neurons. Three clusters corresponding to tumor cells were also removed to focus on immune cells. Principal components analysis was performed again, and the 15 dimensions were used to replot the data. A range of resolutions from 0.2 to 1.0 was used to identify clusters, and data were further processed at a resolution of 0.4. Marker genes for each cluster were identified using the FindAllMarkers function by model-based analysis of single-cell transcriptomics (MAST) using LogNormalized RNA counts. Clusters were annotated according to cell type–specific gene expression, and the proportion of cells in each cluster for each sample was calculated. To perform differential gene expression analysis between ASO and inactive groups, pseudo-bulk matrices of summed counts for each cluster were constructed from $n = 2$ biological replicate scRNA-seq datasets per group. Differential gene expression for each cluster was then determined using the edgeR package. Pathway analysis of up- and down-regulated genes was performed using EnrichR-KG and the TRUSTT, KEGG, and Reactome databases.

The Cancer Genome Atlas data processing

The UCSC xena browser (https://xenabrowser.net/) was used to download relevant dataset for The Cancer Genome Atlas (TCGA) GBM cohort, which included survival, phenotype, and gene expression data profiled in the microarray HGU133 platform and the nonsilent mutation call data. TREM2 mRNA expression in 252 primary GBM tumor samples (*IDH1/2*–wild-type) and 10 normal brain

specimens was plotted (log scale; horizontal line represents median, and dots indicate individual patient's TREM2 expression). The Wilcoxon rank sum test was performed for comparison. The TCGA pan-cancer RNA-seq (v2) normalized TREM2 expression data for low-grade glioma and GBM cohorts were downloaded via UCSC xena browser, including 6 normal, 65 G2 astrocytoma, 77 G2 oligoastrocytoma, 116 G2 oligodendroglioma, 132 G3 astrocytoma, 56 G3 oligoastrocytoma, 82 G3 oligodendroglioma, and 166 GBM patient samples. The Kruskal-Wallis test was used to compare TREM2 expressions across all groups. The PFS data of 249 patients with *IDH1/2*–wild-type GBM were further analyzed on the basis of TREM2 expression. TREM2 expression was dichotomized into high/low by the optimal cutoff. Kaplan-Meier curves were generated for high- and low-expressing patients, and log-rank test was performed. The OS data of patients with *IDH1/2*–wild-type GBM were queried using R package "cgdsr" via cBioPortal (http://www.cbioportal.org/). Kaplan-Meier survival curves were generated for 115 patients with *IDH1/2*–wild-type GBM according to TREM2 expression. Patients were divided into high and low groups based on the optimal cutoff of TREM2 expression, with maximized the log-rank test statistic as implemented in R package "maxstat." Kaplan-Meier curves were shown with the number of events/total *n*, median survival time with 95% confidence interval (CI), hazard ratio with 95% CI, and log-rank test *P* value.

Statistical analysis

Significance assessments were performed with GraphPad Prism 9. A two-tailed Student's *t* test was used for comparisons in experiments with two conditions. One-way analysis of variance (ANOVA) analysis was used for experiments with more than two groups and corrected by Bonferroni test for multiple comparison. Animal survival data were processed into Kaplan-Meier survival curves and performed log-rank tests. All data have been generated from at least three independent biological experiments unless otherwise mentioned. A $P < 0.05$ was considered significant.

Supplementary Materials

This PDF file includes:

Supplementary Materials and Methods
Fig. S1 to S13
Tables S1 to S3
References

View/request a protocol for this paper from *Bio-protocol*.

REFERENCES AND NOTES

1. R. Stupp, M. E. Hegi, W. P. Mason, M. J. van den Bent, M. J. Taphoorn, R. C. Janzer, S. K. Ludwin, A. Allgeier, B. Fisher, K. Belanger, P. Hau, A. A. Brandes, J. Gijtenbeek, C. Marosi, C. J. Vecht, K. Mokhtari, P. Wesseling, S. Villa, E. Eisenhauer, T. Gorlia, M. Weller, D. Lacombe, J. G. Cairncross, R. O. Mirimanoff; on behalf of the European Organisation for Research and Treatment of Cancer Brain Tumour and Radiation Oncology Groups; the National Cancer Institute of Canada Clinical Trials Group, Effects of radiotherapy with concomitant and adjuvant temozolomide versus radiotherapy alone on survival in glioblastoma in a randomised phase III study: 5-year analysis of the EORTC-NCIC trial. *Lancet Oncol.* **10**, 459–466 (2009).
2. R. A. Buerki, Z. S. Chheda, H. Okada, Immunotherapy of primary brain tumors: Facts and hopes. *Clin. Cancer Res.* **24**, 5198–5205 (2018).
3. E. Friebel, K. Kapolou, S. Unger, N. G. Nunez, S. Utz, E. J. Rushing, L. Regli, M. Weller, M. Greter, S. Tugues, M. C. Neidert, B. Becher, Single-cell mapping of human brain cancer reveals tumor-specific instruction of tissue-invading leukocytes. *Cell* **181**, 1626–1642.e20 (2020).
4. F. Klemm, R. R. Maas, R. L. Bowman, M. Kornete, K. Soukup, S. Nassiri, J. P. Brouland, C. A. Iacobuzio-Donahue, C. Brennan, V. Tabar, P. H. Gutin, R. T. Daniel, M. E. Hegi, J. A. Joyce, Interrogation of the microenvironmental landscape in brain tumors reveals disease-specific alterations of immune cells. *Cell* **181**, 1643–1660.e17 (2020).
5. T. K. Ulland, W. M. Song, S. C. Huang, J. D. Ulrich, A. Sergushichev, W. L. Beatty, A. A. Loboda, Y. Zhou, N. J. Cairns, A. Kambal, E. Loginicheva, S. Gilfillan, M. Cella, H. W. Virgin, E. R. Unanue, Y. Wang, M. N. Artyomov, D. M. Holtzman, M. Colonna, TREM2 maintains microglial metabolic fitness in Alzheimer's disease. *Cell* **170**, 649–663.e13 (2017).
6. S. Wang, M. Mustafa, C. M. Yuede, S. V. Salazar, P. Kong, H. Long, M. Ward, O. Siddiqui, R. Paul, S. Gilfillan, A. Ibrahim, H. Rhinn, I. Tassi, A. Rosenthal, T. Schwabe, M. Colonna, Anti-human TREM2 induces microglia proliferation and reduces pathology in an Alzheimer's disease model. *J. Exp. Med.* **217**, e20200785 (2020).
7. S. Krasemann, C. Madore, R. Cialic, C. Baufeld, N. Calcagno, R. El Fatimy, L. Beckers, E. O'Loughlin, Y. Xu, Z. Fanek, D. J. Greco, S. T. Smith, G. Tweet, Z. Humulock, T. Zrzavy, P. Conde-Sanroman, M. Gacias, Z. Weng, H. Chen, E. Tjon, F. Mazaheri, K. Hartmann, A. Madi, J. D. Ulrich, M. Glatzel, A. Worthmann, J. Heeren, B. Budnik, C. Lemere, T. Ikezu, F. L. Heppner, V. Litvak, D. M. Holtzman, H. Lassmann, H. L. Weiner, J. Ochando, C. Haass, O. Butovsky, The TREM2-APOE pathway drives the transcriptional phenotype of dysfunctional microglia in neurodegenerative diseases. *Immunity* **47**, 566–581.e9 (2017).
8. S. M. Kim, E. M. Kim, K. Y. Ji, H. Y. Lee, S. M. Yee, S. M. Woo, J. W. Yi, C. H. Yun, H. Choi, H. S. Kang, TREM2 acts as a tumor suppressor in colorectal carcinoma through Wnt1/beta-catenin and Erk signaling. *Cancer* **11**, 1315 (2019).
9. A. Esparza-Baquer, I. Labiano, O. Sharif, A. Agirre-Lizaso, F. Oakley, P. M. Rodrigues, E. Zhuravleva, C. J. O'Rourke, E. Hijona, R. Jimenez-Aguero, I. Riano, A. Landa, A. La Casta, M. Y. W. Zaki, P. Munoz-Garrido, M. Azkargorta, F. Elortza, A. Vogel, G. Schabbauer, P. Aspichueta, J. B. Andersen, S. Knapp, D. A. Mann, L. Bujanda, J. M. Banales, M. J. Perugorria, TREM-2 defends the liver against hepatocellular carcinoma through multifactorial protective mechanisms. *Gut* **70**, 1345–1361 (2021).
10. H. Y. Zhang, Z. L. Liu, H. Y. Wen, Y. F. Guo, F. K. Xu, Q. L. Zhu, W. Yuan, R. K. Luo, C. L. Lu, R. H. Liu, J. Gu, D. Ge, Immunosuppressive TREM2^{+} macrophages are associated with undesirable prognosis and responses to anti-PD-1 immunotherapy in non-small cell lung cancer. *Cancer Immunol. Immunother.* **71**, 2511–2522 (2022).
11. X. J. Zhang, W. Wang, P. Li, X. D. Wang, K. Ni, High TREM2 expression correlates with poor prognosis in gastric cancer. *Hum. Pathol.* **72**, 91–99 (2018).
12. A. Deczkowska, A. Weiner, I. Amit, The physiology, pathology, and potential therapeutic applications of the TREM2 signaling pathway. *Cell* **181**, 1207–1217 (2020).
13. K. Nakamura, M. J. Smyth, TREM2 marks tumor-associated macrophages. *Signal. Transduct. Target. Ther.* **5**, 233 (2020).
14. M. Binnewies, J. L. Pollack, J. Rudolph, S. Dash, M. Abushawish, T. Lee, N. S. Jahchan, P. Canaday, E. Lu, M. Norng, S. Mankikar, V. M. Liu, X. Y. Du, A. Chen, R. Mehta, R. Palmer, V. Juric, L. D. Liang, K. P. Baker, L. Reyno, M. F. Krummel, M. Streuli, V. Sriram, Targeting TREM2 on tumor-associated macrophages enhances immunotherapy. *Cell Rep.* **37**, 109844 (2021).
15. M. Molgora, E. Esaulova, W. Vermi, J. Hou, Y. Chen, J. Luo, S. Brioschi, M. Bugatti, A. S. Omodei, B. Ricci, C. Fronick, S. K. Panda, Y. Takeuchi, M. M. Gubin, R. Faccio, M. Cella, S. Gilfillan, E. R. Unanue, M. N. Artyomov, R. D. Schreiber, M. Colonna, TREM2 modulation remodels the tumor myeloid landscape enhancing anti-PD-1 immunotherapy. *Cell* **182**, 886–900.e17 (2020).
16. K. Kluckova, J. Kozak, K. Szaboova, B. Rychly, M. Svajdler, M. Suchankova, E. Tibenska, B. Filova, J. Steno, V. Matejcik, M. Homolova, M. Bucova, TREM-1 and TREM-2 expression on blood monocytes could help predict survival in high-grade glioma patients. *Mediators Inflamm.* **2020**, 1798147 (2020).
17. T. Mahlokozera, B. Patel, H. Chen, P. Desouza, X. Qu, D. D. Mao, D. Hafez, W. Yang, R. Taiwo, M. Paturu, A. Salehi, A. D. Gujar, G. P. Dunn, N. Mosammaparast, A. A. Petti, H. Yano, A. H. Kim, Competitive binding of E3 ligases TRIM26 and WWP2 controls SOX2 in glioblastoma. *Nat. Commun.* **12**, 6321 (2021).
18. C. Neftel, J. Laffy, M. G. Filbin, T. Hara, M. E. Shore, G. J. Rahme, A. R. Richman, D. Silverbush, M. L. Shaw, C. M. Hebert, J. Dewitt, S. Gritsch, E. M. Perez, L. N. G. Castro, X. Lan, N. Druck, C. Rodman, D. Dionne, A. Kaplan, M. S. Bertalan, J. Small, K. Pelton, S. Becker, D. Bonal, Q.-D. Nguyen, R. L. Servis, J. M. Fung, R. Mylvaganam, L. Mayr, J. Gojo, C. Haberler, R. Geyeregger, T. Czech, I. Slavc, B. V. Nahed, W. T. Curry, B. S. Carter, H. Wakimoto, P. K. Brastianos, T. T. Batchelor, A. Stemmer-Rachamimov, M. Martinez-Lage, M. P. Frosch, I. Stamenkovic, N. Riggi, E. Rheinbay, M. Monje, O. Rozenblatt-Rosen, D. P. Cahill, A. P. Patel, T. Hunter, I. M. Verma, K. L. Ligon, D. N. Louis, A. Regev, B. E. Bernstein, I. Tirosh, M. L. Suvà, An integrative model of cellular states, plasticity, and genetics for glioblastoma. *Cell* **178**, 835–849.e21 (2019).

19. V. Genoud, E. Marinari, S. I. Nikolaev, J. C. Castle, V. Bukur, P. Y. Dietrich, H. Okada, P. R. Walker, Responsiveness to anti-PD-1 and anti-CTLA-4 immune checkpoint blockade in SB28 and GL261 mouse glioma models. *Onco. Targets. Ther.* **7**, e1501137 (2018).
20. L. B. Garcia, O. Reiners, A. Gonzalez-Junca, H. Okada, M. H. Barcellos-Hoff, Radiation primes Sb28 glioblastoma for response to TGFβ and PD-L1 neutralizing antibodies. *Neuro Oncol.* **21**, vi208 (2019).
21. X. D. Guan, M. N. Hasan, G. Begum, G. Kohanbash, K. E. Carney, V. M. Pigott, A. I. Persson, M. G. Castro, W. Jia, D. D. Sun, Blockade of Na/H exchanger stimulates glioma tumor immunogenicity and enhances combinatorial TMZ and anti-PD-1 therapy. *Cell Death Dis.* **9**, 1010 (2018).
22. V. Letchuman, L. Ampie, A. H. Shah, D. A. Brown, J. D. Heiss, P. Chittiboina, Syngeneic murine glioblastoma models: Reactionary immune changes and immunotherapy intervention outcomes. *Neurosurg. Focus* **52**, E5 (2022).
23. E. F. Simonds, E. D. Lu, O. Badillo, S. Karimi, E. V. Liu, W. Tamaki, C. Rancan, K. M. Downey, J. Stultz, M. Sinha, L. K. McHenry, N. M. Nasholm, P. Chuntova, A. Sundström, V. Genoud, S. A. Shahani, L. D. Wang, C. E. Brown, P. R. Walker, F. J. Swartling, L. Fong, H. Okada, W. A. Weiss, M. Hellström, Deep immune profiling reveals targetable mechanisms of immune evasion in immune checkpoint inhibitor-refractory glioblastoma. *J. Immunother. Cancer* **9**, e002181 (2021).
24. F. J. Nunez, F. M. Mendez, P. Kadiyala, M. S. Alghamri, M. G. Savelieff, M. B. Garcia-Fabiani, S. Haase, C. Koschmann, A. A. Calinescu, N. Kamran, M. Saxena, R. Patel, S. Carney, M. Z. Guo, M. Edwards, M. Ljungman, T. Qin, M. A. Sartor, R. Tagett, S. Venneti, J. Brosnan-Cashman, A. Meeker, V. Gorbunova, L. Zhao, D. M. Kremer, L. Zhang, C. A. Lyssiotis, L. Jones, C. J. Herting, J. L. Ross, D. Hambardzumyan, S. Hervey-Jumper, M. E. Figueroa, P. R. Lowenstein, M. G. Castro, IDH1-R132H acts as a tumor suppressor in glioma via epigenetic up-regulation of the DNA damage response. *Sci. Transl. Med.* **11**, eaaq1427 (2019).
25. K. M. Schoch, L. A. Ezerskiy, M. M. Morhaus, R. N. Bannon, A. D. Sauerbeck, M. Shabsovich, P. Jafar-Nejad, F. Rigo, T. M. Miller, Acute TREM2 reduction triggers increased microglial phagocytosis, slowing amyloid deposition in mice. *Proc. Natl. Acad. Sci. U.S.A.* **118**, e2100356118 (2021).
26. G. Toda, T. Yamauchi, T. Kadowaki, K. Ueki, Preparation and culture of bone marrow-derived macrophages from mice for functional analysis. *STAR Protoc.* **2**, 100246 (2021).
27. J. L. Balligand, D. Ungureanu, R. A. Kelly, L. Kobzik, D. Pimental, T. Michel, T. W. Smith, Abnormal contractile function due to induction of nitric oxide synthesis in rat cardiac myocytes follows exposure to activated macrophage-conditioned medium. *J. Clin. Invest.* **91**, 2314–2319 (1993).
28. A. E. Koch, P. J. Polverini, S. L. Kunkel, L. A. Harlow, L. A. DiPietro, V. M. Elner, S. G. Elner, R. M. Strieter, Interleukin-8 as a macrophage-derived mediator of angiogenesis. *Science* **258**, 1798–1801 (1992).
29. H. Ikeda, L. J. Old, R. D. Schreiber, The roles of IFNγ in protection against tumor development and cancer immunoediting. *Cytokine Growth Factor Rev.* **13**, 95–109 (2002).
30. A. S. Dighe, E. Richards, L. J. Old, R. D. Schreiber, Enhanced in vivo growth and resistance to rejection of tumor cells expressing dominant negative IFN gamma receptors. *Immunity* **1**, 447–456 (1994).
31. Y. Xiao, K. Yang, Z. Wang, M. Zhao, Y. Deng, W. Ji, Y. Zou, C. Qian, Y. Liu, H. Xiao, H. Liu, CD44-mediated poor prognosis in glioma is associated with M2-polarization of tumor-associated macrophages and immunosuppression. *Front. Surg.* **8**, 775194 (2021).
32. E. M. Palsson-McDermott, A. M. Curtis, G. Goel, M. A. R. Lauterbach, F. J. Sheedy, L. E. Gleeson, M. W. M. van den Bosch, S. R. Quinn, R. Domingo-Fernandez, D. G. W. Johnston, J. Jiang, W. J. Israelsen, J. Keane, C. Thomas, C. Clish, M. V. Heiden, R. J. Xavier, L. A. J. O'Neill, Pyruvate kinase M2 regulates Hif-1α activity and IL-1β induction and is a critical determinant of the Warburg effect in LPS-activated macrophages. *Cell Metab.* **21**, 65–80 (2015).
33. S. Zilio, S. Bicciato, D. Weed, P. Serafini, CCR1 and CCR5 mediate cancer-induced myelopoiesis and differentiation of myeloid cells in the tumor. *J. Immunother. Cancer* **10**, e003131 (2022).
34. B. Halvorsen, M. Z. Espeland, G. Ø. Andersen, A. Yndestad, E. L. Sagen, A. Rashidi, E. C. Knudsen, M. Skjelland, K. R. Skagen, K. Krohg-Sørensen, S. Holm, V. Ritschel, K. B. Holven, E. A. L. Biessen, P. Aukrust, T. B. Dahl, Increased expression of NAMPT in PBMC from patients with acute coronary syndrome and in inflammatory M1 macrophages. *Atherosclerosis* **243**, 204–210 (2015).
35. P. Yang, H. Qin, Y. Li, A. Xiao, E. Zheng, H. Zeng, C. Su, X. Luo, Q. Lu, M. Liao, L. Zhao, L. Wei, Z. Varghese, J. F. Moorhead, Y. Chen, X. Z. Ruan, CD36-mediated metabolic crosstalk between tumor cells and macrophages affects liver metastasis. *Nat. Commun.* **13**, 5782 (2022).
36. K. D. Bruce, S. Gorkhali, K. Given, A. M. Coates, K. E. Boyle, W. B. Macklin, R. H. Eckel, Lipoprotein lipase is a feature of alternatively-activated microglia and may facilitate lipid uptake in the CNS during demyelination. *Front. Mol. Neurosci.* **11**, 57 (2018).
37. D. D. Mao, A. D. Gujar, T. Mahlokozera, I. Chen, Y. Pan, J. Luo, T. Brost, E. A. Thompson, A. Turski, E. C. Leuthardt, G. P. Dunn, M. R. Chicoine, K. M. Rich, J. L. Dowling, G. J. Zipfel, R. G. Dacey, S. Achilefu, D. D. Tran, H. Yano, A. H. Kim, A CDC20-APC/SOX2 signaling axis regulates human glioblastoma stem-like cells. *Cell Rep.* **11**, 1809–1821 (2015).
38. X. Q. Wang, B. B. Tao, B. Li, X. H. Wang, W. C. Zhang, L. Wan, X. M. Hua, S. T. Li, Overexpression of TREM2 enhances glioma cell proliferation and invasion: A therapeutic target in human glioma. *Oncotarget* **7**, 2354–2366 (2016).
39. J. Auwerx, The human leukemia cell line, THP-1: A multifacetted model for the study of monocyte-macrophage differentiation. *Experientia* **47**, 22–31 (1991).
40. I. R. Turnbull, S. Gilfillan, M. Cella, T. Aoshi, M. Miller, L. Piccio, M. Hernandez, M. Colonna, Cutting edge: TREM-2 attenuates macrophage activation. *J. Immunol.* **177**, 3520–3524 (2006).
41. G. J. Adema, F. Hartgers, R. Verstraten, E. de Vries, G. Marland, S. Menon, J. Foster, Y. Xu, P. Nooyen, T. McClanahan, K. B. Bacon, C. G. Figdor, A dendritic-cell-derived C-C chemokine that preferentially attracts naive T cells. *Nature* **387**, 713–717 (1997).
42. C. Chenivesse, Y. Chang, I. Azzaoui, S. Ait Yahia, O. Morales, C. Ple, A. Foussat, A. B. Tonnel, N. Delhem, H. Yssel, H. Vorng, B. Wallaert, A. Tsicopoulos, Pulmonary CCL18 recruits human regulatory T cells. *J. Immunol.* **189**, 128–137 (2012).
43. Q. Li, Z. Cheng, L. Zhou, S. Darmanis, N. F. Neff, J. Okamoto, G. Gulati, M. L. Bennett, L. O. Sun, L. E. Clarke, J. Marschallinger, G. Yu, S. R. Quake, T. Wyss-Coray, B. A. Barres, Developmental heterogeneity of microglia and brain myeloid cells revealed by deep single-cell RNA sequencing. *Neuron* **101**, 207–223.e10 (2019).
44. A. Henn, S. Lund, M. Hedtjarn, A. Schrattenholz, P. Porzgen, M. Leist, The suitability of BV2 cells as alternative model system for primary microglia cultures or for animal experiments examining brain inflammation. *ALTEX* **26**, 83–94 (2009).
45. S. Schildge, C. Bohrer, K. Beck, C. Schachtrup, Isolation and culture of mouse cortical astrocytes. *J. Vis. Exp.*, 50079 (2013).
46. W. Zou, J. D. Wolchok, L. Chen, PD-L1 (B7-H1) and PD-1 pathway blockade for cancer therapy: Mechanisms, response biomarkers, and combinations. *Sci. Transl. Med.* **8**, 328rv324 (2016).
47. B. J. Andreone, L. Przybyla, C. Llapashtica, A. Rana, S. S. Davis, B. van Lengerich, K. Lin, J. Shi, Y. Mei, G. Astarita, G. D. Paolo, T. Sandmann, K. M. Monroe, J. W. Lewcock, Alzheimer's-associated PLCγ2 is a signaling node required for both TREM2 function and the inflammatory response in human microglia. *Nat. Neurosci.* **23**, 927–938 (2020).
48. D. Daley, V. R. Mani, N. Mohan, N. Akkad, A. Ochi, D. W. Heindel, K. B. Lee, C. P. Zambirinis, G. S. B. Pandian, S. Savadkar, A. Torres-Hernandez, S. Nayak, D. Wang, M. Hundeyin, B. Diskin, B. Aykut, G. Werba, R. M. Barilla, R. Rodriguez, S. Chang, L. Gardner, L. K. Mahal, B. Ueberheide, G. Miller, Dectin 1 activation on macrophages by galectin 9 promotes pancreatic carcinoma and peritumoral immune tolerance. *Nat. Med.* **23**, 556–567 (2017).
49. M. L. Wang, M. Motamed, R. E. Infante, L. Abi-Mosleh, H. J. Kwon, M. S. Brown, J. L. Goldstein, Identification of surface residues on Niemann-Pick C2 essential for hydrophobic handoff of cholesterol to NPC1 in lysosomes. *Cell Metab.* **12**, 166–173 (2010).
50. C. Zhang, N. Bai, A. Chang, Z. Zhang, J. Yin, W. Shen, Y. Tian, R. Xiang, C. Liu, ATF4 is directly recruited by TLR4 signaling and positively regulates TLR4-trigged cytokine production in human monocytes. *Cell. Mol. Immunol.* **10**, 84–94 (2013).
51. B. Zou, J. Liu, D. J. Klionsky, D. Tang, R. Kang, Extracellular SQSTM1 as an inflammatory mediator. *Autophagy* **16**, 2313–2315 (2020).
52. H. M. Marriott, C. D. Bingle, R. C. Read, K. E. Braley, G. Kroemer, P. G. Hellewell, R. W. Craig, M. K. B. Whyte, D. H. Dockrell, Dynamic changes in Mcl-1 expression regulate macrophage viability or commitment to apoptosis during bacterial clearance. *J. Clin. Invest.* **115**, 359–368 (2005).
53. S. J. Korsmeyer, J. R. Shutter, D. J. Veis, D. E. Merry, Z. N. Oltvai, Bcl-2/Bax: A rheostat that regulates an anti-oxidant pathway and cell death. *Semin. Cancer Biol.* **4**, 327–332 (1993).
54. J. I. Fletcher, S. Meusburger, C. J. Hawkins, D. T. Riglar, E. F. Lee, W. D. Fairlie, D. C. Huang, J. M. Adams, Apoptosis is triggered when prosurvival Bcl-2 proteins cannot restrain Bax. *Proc. Natl. Acad. Sci. U.S.A.* **105**, 18081–18087 (2008).
55. T. Frömel, K. Kohlstedt, R. Popp, X. Yin, K. Awwad, E. Barbosa-Sicard, A. C. Thomas, R. Lieberz, M. Mayr, I. Fleming, Cytochrome P4502S1: A novel monocyte/macrophage fatty acid epoxygenase in human atherosclerotic plaques. *Basic Res. Cardiol.* **108**, 319 (2013).
56. A. R. Pombo Antunes, I. Scheyltjens, F. Lodi, J. Messiaen, A. Antoranz, J. Duerinck, D. Kancheva, L. Martens, K. De Vlaminck, H. Van Hove, S. S. Kjolner Hansen, F. M. Bosisio, K. Van der Borght, S. De Vleeschouwer, R. Sciot, L. Bouwens, M. Verfaillie, N. Vandamme, R. E. Vandenbroucke, O. De Wever, Y. Saeys, M. Guilliams, C. Gysemans, B. Neyns, F. De Smet, D. Lambrechts, J. A. Van Ginderachter, K. Movahedi, Single-cell profiling of myeloid cells in glioblastoma across species and disease stage reveals macrophage competition and specialization. *Nat. Neurosci.* **24**, 595–610 (2021).
57. R. Dagher, A. M. Copenhaver, V. Besnard, A. Berlin, F. Hamidi, M. Maret, J. Wang, X. Qu, Y. Shrestha, J. Wu, G. Gautier, R. Raja, M. Aubier, R. Kolbeck, A. A. Humbles, M. Pretolani, IL-33-ST2 axis regulates myeloid cell differentiation and activation enabling effective club cell regeneration. *Nat. Commun.* **11**, 4786 (2020).

58. H. Sato, Y. Taketomi, Y. Miki, R. Murase, K. Yamamoto, M. Murakami, Secreted phospholipase PLA2G2D contributes to metabolic health by mobilizing ω3 polyunsaturated fatty acids in WAT. *Cell Rep.* **31**, 107579 (2020).
59. Y. Ber, R. Shiloh, Y. Gilad, N. Degani, S. Bialik, A. Kimchi, DAPK2 is a novel regulator of mTORC1 activity and autophagy. *Cell Death Differ.* **22**, 465–475 (2015).
60. W. Hartmann, B. J. Marsland, B. Otto, J. Urny, B. Fleischer, S. Korten, A novel and divergent role of granzyme A and B in resistance to helminth infection. *J. Immunol.* **186**, 2472–2481 (2011).
61. T. Z. Hou, J. Bystrom, J. P. Sherlock, O. Qureshi, S. M. Parnell, G. Anderson, D. W. Gilroy, C. D. Buckley, A distinct subset of podoplanin (gp38) expressing F4/80^{+} macrophages mediate phagocytosis and are induced following zymosan peritonitis. *FEBS Lett.* **584**, 3955–3961 (2010).
62. G. Solinas, S. Schiarea, M. Liguori, M. Fabbri, S. Pesce, L. Zammataro, F. Pasqualini, M. Nebuloni, C. Chiabrando, A. Mantovani, P. Allavena, Tumor-conditioned macrophages secrete migration-stimulating factor: A new marker for M2-polarization, influencing tumor cell motility. *J. Immunol.* **185**, 642–652 (2010).
63. I. Müller, T. Schönberger, M. Schneider, O. Borst, M. Ziegler, P. Seizer, C. Leder, K. Müller, M. Lang, F. Appenzeller, O. Lunov, B. Büchele, M. Fahrleitner, M. Olbrich, H. Langer, T. Geisler, F. Lang, M. Chatterjee, J. F. de Boer, U. J. F. Tietge, J. Bernhagen, T. Simmet, M. Gawaz, Gremlin-1 is an inhibitor of macrophage migration inhibitory factor and attenuates atherosclerotic plaque growth in ApoE$^{-/-}$ mice. *J. Biol. Chem.* **288**, 31635–31645 (2013).
64. A. Nott, I. R. Holtman, N. G. Coufal, J. C. M. Schlachetzki, M. Yu, R. Hu, C. Z. Han, M. Pena, J. Xiao, Y. Wu, Z. Keulen, M. P. Pasillas, C. O'Connor, C. K. Nickl, S. T. Schafer, Z. Shen, R. A. Rissman, J. B. Brewer, D. Gosselin, D. D. Gonda, M. L. Levy, M. G. Rosenfeld, G. McVicker, F. H. Gage, B. Ren, C. K. Glass, Brain cell type-specific enhancer-promoter interactome maps and disease-risk association. *Science* **366**, 1134–1139 (2019).
65. L. L. Fu, M. Yan, M. X. Ma, Y. Luo, M. Shao, M. Gosau, R. E. Friedrich, T. Vollkommer, H. C. Feng, R. Smeets, DCBLD1 overexpression is associated with a poor prognosis in head and neck squamous cell carcinoma. *Front. Immunol.* **13**, 939344 (2022).
66. A. F. Haddad, J. S. Young, D. Amara, M. S. Berger, D. R. Raleigh, M. K. Aghi, N. A. Butowski, Mouse models of glioblastoma for the evaluation of novel therapeutic strategies. *Neurooncol. Adv.* **3**, vdab100 (2021).
67. L. B. Ivashkiv, IFNγ: Signalling, epigenetics and roles in immunity, metabolism, disease and cancer immunotherapy. *Nat. Rev. Immunol.* **18**, 545–558 (2018).
68. M. Chawla-Sarkar, D. J. Lindner, Y. F. Liu, B. R. Williams, G. C. Sen, R. H. Silverman, E. C. Borden, Apoptosis and interferons: Role of interferon-stimulated genes as mediators of apoptosis. *Apoptosis* **8**, 237–249 (2003).
69. N. Su, Y. Li, J. Wang, J. Fan, X. Li, W. Peng, X. Yu, T. B. Zhou, Z. Jiang, Role of MAPK signal pathways in differentiation process of M2 macrophages induced by high-ambient glucose and TGF-β1. *J. Recept. Signal Transduct. Res.* **35**, 396–401 (2015).
70. D. Baumann, J. Drebant, T. Hagele, L. Burger, C. Serger, C. Lauenstein, P. Dudys, G. Erdmann, R. Offringa, p38 MAPK signaling in M1 macrophages results in selective elimination of M2 macrophages by MEK inhibition. *J. Immunother. Cancer* **9**, e002319 (2021).
71. M. S. Han, D. Y. Jung, C. Morel, S. A. Lakhani, J. K. Kim, R. A. Flavell, R. J. Davis, JNK expression by macrophages promotes obesity-induced insulin resistance and inflammation. *Science* **339**, 218–222 (2013).
72. G. L. Schieven, The biology of p38 kinase: A central role in inflammation. *Curr. Top. Med. Chem.* **5**, 921–928 (2005).
73. J. M. Park, F. R. Greten, A. Wong, R. J. Westrick, J. S. Arthur, K. Otsu, A. Hoffmann, M. Montminy, M. Karin, Signaling pathways and genes that inhibit pathogen-induced macrophage apoptosis—CREB and NF-κB as key regulators. *Immunity* **23**, 319–329 (2005).
74. V. N. Sukhorukov, V. A. Khotina, Y. S. Chegodaev, E. Ivanova, I. A. Sobenin, A. N. Orekhov, Lipid metabolism in macrophages: Focus on atherosclerosis. *Biomedicine* **8**, 262 (2020).
75. D. A. Jaitin, L. Adlung, C. A. Thaiss, A. Weiner, B. Li, H. Descamps, P. Lundgren, C. Bleriot, Z. Liu, A. Deczkowska, H. Keren-Shaul, E. David, N. Zmora, S. M. Eldar, N. Lubezky, O. Shibolet, D. A. Hill, M. A. Lazar, M. Colonna, F. Ginhoux, H. Shapiro, E. Elinav, I. Amit, Lipid-associated macrophages control metabolic homeostasis in a Trem2-dependent manner. *Cell* **178**, 686–698.e14 (2019).
76. R. Y. Li, Q. Qin, H. C. Yang, Y. Y. Wang, Y. X. Mi, Y. S. Yin, M. Wang, C. J. Yu, Y. Tang, TREM2 in the pathogenesis of AD: A lipid metabolism regulator and potential metabolic therapeutic target. *Mol. Neurodegener.* **17**, 40 (2022).
77. E. Timperi, P. Gueguen, M. Molgora, I. Magagna, Y. Kieffer, S. Lopez-Lastra, P. Sirven, L. G. Baudrin, S. Baulande, A. Nicolas, G. Champenois, D. Meseure, A. Vincent-Salomon, A. Tardivon, E. Laas, V. Soumelis, M. Colonna, F. Mechta-Grigoriou, S. Amigorena, E. Romano, Lipid-associated macrophages are induced by cancer-associated fibroblasts and mediate immune suppression in breast cancer. *Cancer Res.* **82**, 3291–3306 (2022).
78. A. K. Y. Yim, P. L. Wang, J. R. Bermingham Jr., A. Hackett, A. Strickland, T. M. Miller, C. Ly, R. D. Mitra, J. Milbrandt, Disentangling glial diversity in peripheral nerves at single-nuclei resolution. *Nat. Neurosci.* **25**, 238–251 (2022).
79. L. Song, S. Pan, Z. Zhang, L. Jia, W. Chen, X. Zhao, STAB: A spatio-temporal cell atlas of the human brain. *Nucleic Acids Res.* **49**, D1029–D1037 (2021).
80. S. M. Pollard, K. Yoshikawa, I. D. Clarke, D. Danovi, S. Stricker, R. Russell, J. Bayani, R. Head, M. Lee, M. Bernstein, J. A. Squire, A. Smith, P. Dirks, Glioma stem cell lines expanded in adherent culture have tumor-specific phenotypes and are suitable for chemical and genetic screens. *Cell Stem Cell* **4**, 568–580 (2009).

Acknowledgments: We thank H. Okada (UCSF) for providing the SB28 cell line and M. G. Castro (University of Michigan Medical School) for providing the NPA C54B (NRAS/shTP53/shATRX) cell line. We thank members of A.H.K. and H.Y. laboratories for helpful discussions. **Funding:** This work was supported by National Institutes of Health grants R01 NS106612 (to A.H.K), the Alvin J. Siteman Cancer Center Siteman Investment Program through funding from The Foundation for Barnes-Jewish Hospital (to A.H.K.), the Christopher Davidson and Knight Family Fund (to A.H.K.), and the Duesenberg Research Fund (to A.H.K.). **Author contributions:** R.S. designed and performed most of the experiments. R.H., A.Y., and H.J. helped with animal experiments. J.D.U., C.M., S.K., R.S., and J.L. analyzed the scRNA-seq, bulk RNA-seq, and TCGA data. G.T.T. and Y.C. helped with cellular experiments. K.M.S. and T.M.M. guided the ASO in vivo experiment. J.H. and Y.C. generated and purified anti-TREM2 antibody (clone: 178). D.D.M. established human GSC lines. R.C. maintained the animal surgery platform. Q.L., A.P., and D.M.H. offered valuable resources and critical suggestions. R.S. drafted and revised the manuscript. D.M.H. and A.H.K. reviewed, edited, and revised the manuscript. A.H.K. supervised and acquired the funding. **Competing interests:** R.S., T.M.M., D.M.H., and A.H.K. declare that they are listed as the inventors of a provisional patent application, derived from findings in this manuscript, and filed to the U.S. Patent and Trademark Office. This patent was filed on 3 April 2023 by C. VanEngelen in the Office of Technology Management/Tech Transfer, Washington University (application #63/493,830). A.H.K. is a consultant for Monteris Medical. D.M.H. is as an inventor on a patent licensed by Washington University to C2N Diagnostics on the therapeutic use of anti-tau antibodies and a patent licensed to NextCure on the therapeutic use of anti–apolipoprotein E antibodies. D.M.H. co-founded and is on the scientific advisory board of C2N Diagnostics. D.M.H. is on the scientific advisory board of Denali, Genentech, and Cajal Neuroscience and consults for Alector. T.M.M. is a consultant for Biogen, Ionis Pharmaceuticals, Cytokinetics, UCB, and Bioio and is part of a licensing agreement with C2N and Ionis Pharmaceuticals. All other authors declare that they have no competing interests. **Data and materials availability:** All data needed to evaluate the conclusions in the paper are present in the paper and /or the Supplementary Materials. Raw data for the scRNA-seq of in vivo SB28 tumors from ASO-treated mice and bulk RNA-seq of primary mouse BMDMs and microglia have been deposited in GEO (GSE226172).

Submitted 10 August 2022
Accepted 7 April 2023
Published 12 May 2023
10.1126/sciadv.ade3559